AGU ADVANCING EARTH AND SPACE SCIENCE

Key Points:

- We propose an improved critical relative humidity (RH_c) formula that incorporates geographic dependence and allows for non-monotonic variations in the vertical
- Varying RH_c and techniques in calculating subgrid condensation replicates the range of uncertainty found in Coupled Model Intercomparison Project Phase 6 cloud feedback estimates
- Varying RH_c and its implementation in models leads to the diversity of cloud feedback being mainly due to optically thick clouds

Correspondence to:
X. Wang,
wangxc@lasg.iap.ac.cn

The Use of Satellite Data-Based "Critical Relative Humidity" in Cloud Parameterization and Its Role in Modulating Cloud Feedback

Xiaocong Wang[1] , Hao Miao[2], Yimin Liu[1] , Qing Bao[1] , Bian He[1] , Jinxiao Li[1] , and Yaxin Zhao[1]

[1]State Key Laboratory of Numerical Modeling for Atmospheric Sciences and Geophysical Fluid Dynamics (LASG), Institute of Atmospheric Physics (IAP), Chinese Academy of Sciences (CAS), Beijing, China, [2]Key Laboratory of Transportation Meteorology of China Meteorological Administration, Nanjing Joint Institute for Atmospheric Sciences, Nanjing, China

Abstract The critical relative humidity (RH_c), which approximately measures the subgrid-scale variability of moisture, is important to cloud parameterization. Based on the diagnostics from CloudSat/CALIPSO satellite data, we propose an improved RH_c formula that incorporates geographic dependence and allows for non-monotonic variations in the vertical. With the parameterized RH_c, a cloud macrophysics scheme is constructed in which fractional cloudiness and subgrid-scale condensation are synergistically solved, with the latter being calculated using two different approaches. Results show the new scheme largely alleviates the underestimation of high- and mid-level clouds in the default model. The performance is also superior to the simulations applying a globally uniform RH_c as conventionally used in the literature. Varying RH_c and the techniques for computing subgrid-scale condensation leads to a marked diversity in cloud feedback, which nearly replicates the range of uncertainty found in Coupled Model Intercomparison Project Phase 6 models. Using smaller RH_c leads to larger spread than using larger ones. And the spread caused by different techniques for calculating subgrid-scale condensation is larger than that caused by the choice of RH_c. While many previous studies have emphasized the diversity of cloud feedback due to low clouds, varying RH_c and its implementation leads to diversity of cloud feedback being mainly due to optically thick clouds. These results highlight the importance of RH_c in inducing uncertainty of cloud feedback, as well as notes of caution to modelers when using RH_c to tune models.

Plain Language Summary To represent subgrid-scale cloud condensation in climate models, information on fluctuations of temperature and moisture within a grid is indispensable. By neglecting temperature fluctuations and assuming that the probability density function of total water is uniform, the subgrid-scale variability of moisture is reduced to the so-called "critical relative humidity" (RH_c). Previous parameterizations assume RH_c is globally uniform and varying monotonically in the vertical, which is far from realistic. Based on the diagnostics from CloudSat/CALIPSO satellite data, we propose an improved RH_c formula that incorporates geographic dependence and allows for non-monotonic variations in the vertical. A RH_c-based cloud macrophysics scheme is then constructed to investigate the role of RH_c on cloudiness simulation and cloud feedback. Results show varying RH_c and the techniques in calculating subgrid-scale condensation nearly replicates the range of uncertainty found in CMIP6 cloud feedback estimates, thus raising caveats for modelers given that RH_c is commonly used as a knob for model tuning.

1. Introduction

It is widely recognized that the simulation of clouds remains an important source of uncertainty in climate modeling, despite tremendous progresses having been made in the last few decades (Bony & Emanuel, 2001; Cheng & Xu, 2006, 2015; Golaz et al., 2002; Larson et al., 2012; Neggers, 2009; Qin et al., 2018; Tompkins, 2002). The challenge arises because clouds form at scales typically smaller than those of grid boxes in general circulation models (GCMs), and thus there is a need to represent cloud condensation on subgrid scales, which touches upon the fluctuations of temperature and moisture within a grid.

The essence of a statistical scheme is to derive cloudiness analytically by assuming subgrid-scale fluctuations follow a given probability distribution function (PDF). This has inspired the development of a series of schemes, with the complexity of the PDF forms varying considerably between each other. The simplest one is the empirical

scheme of Sundqvist (1978), which can be equivalently derived by assuming a uniform PDF for total water. The Cloud Layers Unified by Binormals scheme is perhaps the most complex among all, which assumes binormal PDFs jointly for vertical velocities and conserved scalars (Golaz et al., 2002). While complex PDFs are mathematically appealing, they become less attractive owing to increased computational cost and the difficulty in acquiring higher-order moments. Cheng and Xu (2015) proposed a simplified intermediately prognostic higher-order turbulence closure that diagnoses rather than predicts high-order moments, thus significantly reducing the computational cost whilst not degrading the performance. On the other hand, schemes based on simple PDFs, such as uniform and triangular distributions, give fairly realistic simulations while not apparently increasing the model complexity. In most cases, it turns out that it is the statistical moments, rather than PDF forms themselves, that are more important to cloud simulation (Lin, 2014; Wang et al., 2015).

Because models still struggle to accurately represent subgrid-scale processes such as boundary layer turbulence and shallow/deep convection (Xie et al., 2018), the statistical moments derived from GCMs are commonly different from those in observations (Quaas, 2012; Van Weverberg et al., 2016), leading to errors carried over into the cloud simulation. In recent years, high-resolution observations have been used to reveal the subgrid variability in nature. For instance, Lin (2014) compared the subgrid variability of relative humidity at tropical and midlatitude sites using an extensive high-resolution sounding array. Van Weverberg et al. (2016) explored the subgrid variability of temperature and moisture based on ground-based Raman lidar measurements. There are also numerous studies in the literature that investigated subgrid variability using cloud-resolving model or large-eddy model simulations (e.g., Wang et al., 2015; Xu & Krueger, 1991).

For schemes like Sundqvist's that assume a uniform PDF for total water, a more intuitive measure of subgrid variability is the so-called "critical relative humidity" (RH_c), which is formulated as a function of PDF width and the saturation specific humidity. Physically, it represents a threshold of relative humidity that must be reached for clouds to start forming. Quaas (2012; hereafter referred to as Q12) diagnosed RH_c from satellite measurements and obtained a fitting formula based on the globally averaged profile. By applying the new RH_c in the cloudiness formula, he found a 30% increase in cloud feedback compared to the standard version, yet some uncertainty remained due to the use of the "cloud forcing" technique that contains feedback from cloud masking of the clear-sky response rather than clouds alone (Soden et al., 2008; Zhang et al., 1994). In addition to the impact of RH_c on cloud cover, there are also issues regarding how it influences the subgrid-scale condensation process, which has been rarely studied in the literature. Considering the influence of RH_c on both cloud fraction and condensate is more relevant to current GCMs. Regarding the parameterization of RH_c, a globally uniform profile used in previous studies fails to capture the real geographic distribution. Moreover, the vertical structure described as monotonically decreasing from the surface to the top of the atmosphere (TOA) is far from realistic. To this end, it is desirable to propose a new RH_c formula that incorporates the geographic dependence and characterizes the vertical structure with more accuracy. By constructing a RH_c-based cloud macrophysics scheme in which fractional cloudiness and subgrid-scale condensation are synergistically solved, this study aims to answer the following questions: (a) To what extent do simulations using a more accurate RH_c differ from those using a globally averaged one? (b) How different is a simulation that applies RH_c in both cloudiness and condensate from one that applies it in cloudiness alone? And how sensitive is the estimated cloud feedback to such changes? Answering these questions will be helpful toward a better understanding of the sources of cloud feedback uncertainty, and may also shed light on the pathways toward improvement of cloud modeling.

The remainder of this paper is organized as follows. Section 2 diagnoses and parameterizes RH_c based on a combination of satellite measurements and reanalysis. Section 3 describes the model used, the design of the cloud scheme, and the experiments performed. Section 4 evaluates the performance of the new scheme and explores the sensitivity of cloud simulation to different RH_c choices. Section 5 analyzes the cloud feedback under different RH_c configurations, as well as the contributions of specific cloud types to the cloud feedback. And finally, Section 6 gives our conclusions.

2. Diagnosis and Parameterization of RH_c

2.1. Climatological RH_c in Observations

Assuming subgrid-scale fluctuations of total water q_t follow a uniform PDF, and neglecting temperature fluctuations, one arrives at the following formula for the cloud fraction C:

$$C = \begin{cases} 1 - \sqrt{\dfrac{1 - RH}{1 - RH_c}}, & RH > RH_c \\ \\ 0, & RH \leq RH_c \end{cases} \tag{1}$$

where RH represents the grid-box-mean relative humidity. RH_c is the critical relative humidity, defined as

$$RH_c = 1 - \frac{\Delta q}{q_s} \tag{2}$$

where q_s stands for saturation specific humidity, and Δq is half the PDF width satisfying $\Delta q = \sqrt{3}\sigma$, in which σ denotes the standard deviation of q_t. While cloud fraction expressed in Equation 1 is limited by many idealized assumptions and is not universally valid (Xu & Randall, 1996b), the concept behind it helps introduce the key intuitive parameter (i.e., RH_c) that controls the subgrid-scale cloud condensation.

Equation 2 provides a direct way to calculate RH_c from high-resolution observations, as conducted by Van Weverberg et al. (2016). Although the method is simple and straightforward, the derived RH_c is susceptible to the inherent noise of the instrument.

An alternative approach is to inversely derive RH_c from Equation 1, as used in Q12,

$$RH_c = 1 - \frac{1 - RH}{(1 - C)^2} \tag{3}$$

given the cloud fraction C is known. It is worth noting that an additional constraint between RH an C in Equation 3 must be satisfied to ensure that the derived RH_c is in the range of 0~100%. We apply Equation 3 to diagnose RH_c, with the cloudiness observations from CloudSat/CALIPSO (Cloud–Aerosol Lidar and Infrared Pathfinder Satellite Observations), which is the same as described in Miao et al. (2019). Specifically, to determine whether a pixel is cloudy or not, we use a combination of fields of *CPR_Cloud_mask* and *Radar_Reflectivity* fields from 2B-GEOPROF and *CloudFraction* from 2B-GEOPROF-LIDAR. Following Barker (2008), each volume is classified as a cloud if one of the two conditions are satisfied: (a) *CPR_Cloud_mask* ≥ 20 and *Radar_ Reflectivity* ≥ −30 dBz or (b) *CloudFraction* ≥ 99%. The main difference between cloudiness used in this study and that in Q12 is that the former utilizes both radar and lidar information, while the later uses the lidar information only. We then use a horizontal resolution of 2.5 × 2.5° and a vertical resolution of 25 hPa as the standard grid size to derive cloud fraction and grid-box RH, which comes from contemporary reanalysis in the ECMWF (European Center for Medium-Range Weather Forecasts)-AUX product. The relative humidity is calculated according to the algorithm in ECMWF: with respect to water for temperatures above 0°C, with respect to ice for temperatures below −23°C, and a quadratic interpolation of the two in transition range. The procedure is conducted below 100 hPa, given that retrievals of relative humidity become less accurate for the low specific huminites in the upper troposphere (Fetzer et al., 2008; Read et al., 2007). The diagnostics apply to each day at each layer in the vertical dimension, with the climatological RH_c obtained by averaging the values diagnosed on each day during the period 2007–2010. Given that RH_c varies greatly with time and environmental conditions, an optimal RH_c can be obtained using least squares error analysis by minimizing the cost function, as follows:

$$f = \sqrt{\frac{1}{N} \sum_{i=1}^{N} \left(1 - \sqrt{\frac{1 - RH}{1 - RH_c}} - C^{\text{obs}} \right)^2} \tag{4}$$

where N is the total number of samples at each location during the whole period.

Figure 1 shows the geographical distribution of the climatological RH_c at selected levels (200, 500, 700, and 900 hPa) using the averaging and optimal methods. Both results show lower RH_c values in the subtropics and higher ones in the inner tropics, corresponding to larger and smaller subgrid-scale variability in these regions, respectively. In general, the patterns of the two sets of derived RH_c are similar, but the values obtained using the optimal method are systematically larger than those using the average method. RH_c tends to be lower over ocean than over land. Large values of RH_c are found near the surface and in upper layers, with relatively small
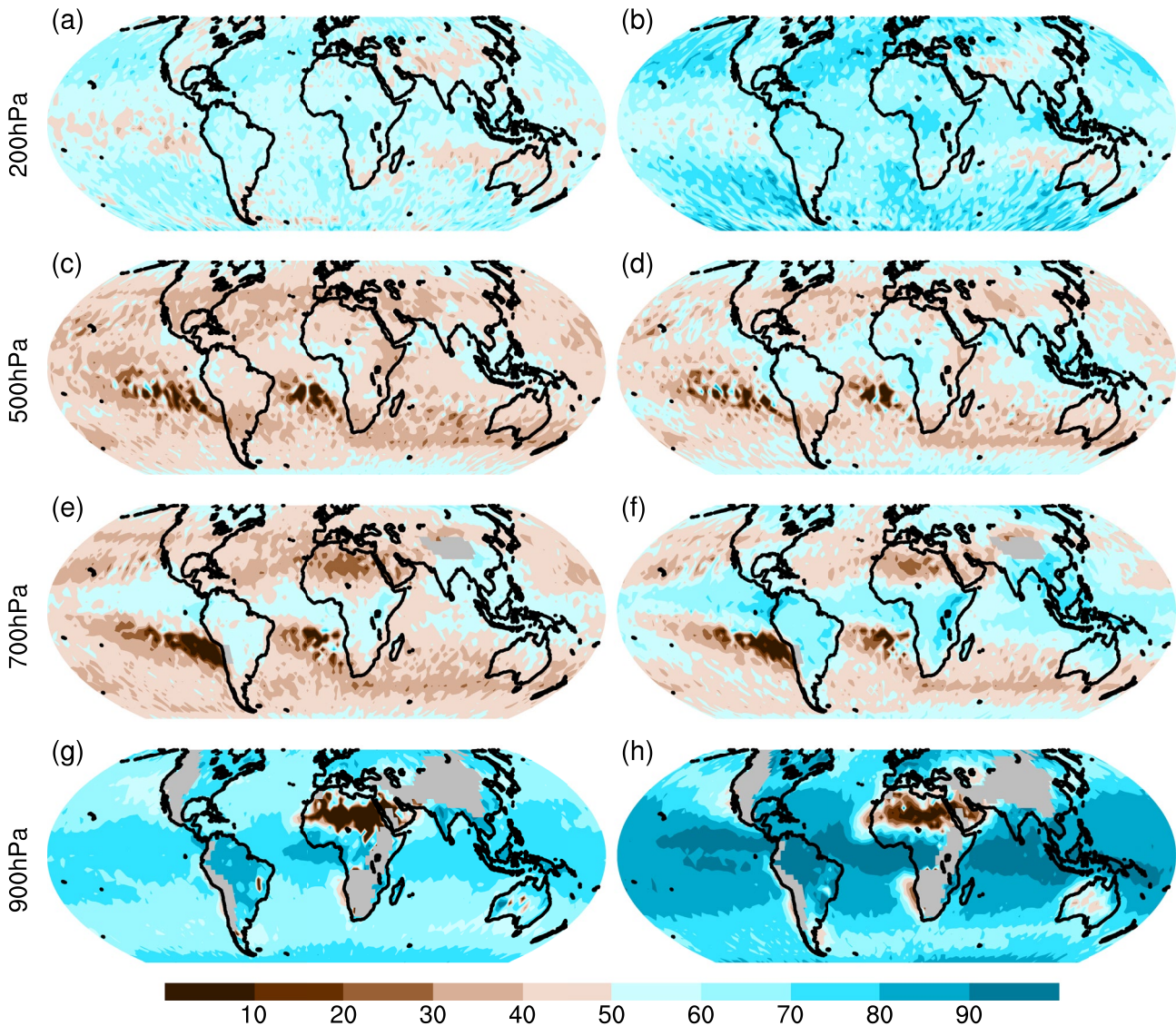
Figure 1. Geographical distribution of CloudSat/CALIPSO diagnostic critical relative humidity (RH_c) (%) at selected pressure levels using the temporal average (left) and least squares method (right).

ones in the middle layers. These findings are generally in good agreement with those of Q12 and Kahn and Teixeira (2009), despite the different observations used.

The vertically varying structure of RH_c is more evident in the latitude–pressure cross section shown in Figure 2. In the vertical, RH_c generally decreases from the surface to the mid-levels and then increases at high levels. On variation with latitude, RH_c decreases from the polar regions to the mid-latitudes, and then slowly increases at the inner tropics. While RH_c reaches its maximum at 300 hPa in the polar regions, it maximizes at the surface and exhibits a second peak at high levels in the other regions. A scatterplot of the two sets of derived RH_c is shown in Figure 2c, where the points collapse reasonably well on a line with a slope of 1.24, indicating the RH_c obtained using the optimal method is nearly 1.24 times of that using the averaging method. For the parameterization of RH_c in the following, the results from the optimal method are used.
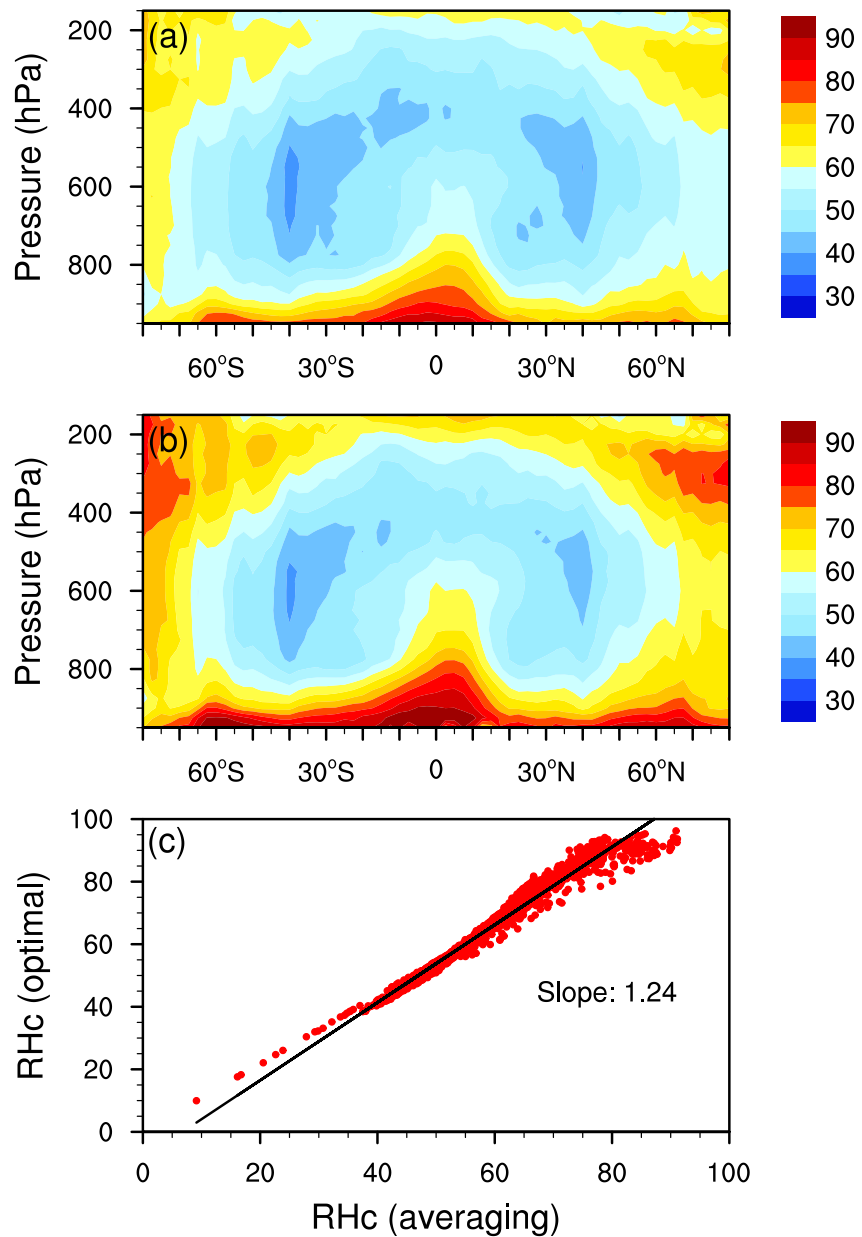
Figure 2. Latitude–pressure cross-section of the zonal mean critical relative humidity (RH$_c$) (%) derived using (a) the temporal average and (b) the least squares method. (c) Scatterplot of the temporal average (*x*-axis) versus least squares method (*y*-axis).

2.2. Parameterization of RH$_c$

Given the approximate symmetry of RH$_c$ in the two hemispheres, RH$_c$ was first symmetrized and then divided into four representative regions (Figure 3a), corresponding respectively to the inner tropics, subtropics, mid-latitudes, and polar regions. In each region, RH$_c$ has the general form:

$$\text{RH}_c = \beta_1 + \beta_2 \times \exp\left[1 - \left(\frac{P}{P_s}\right)^{\beta_3}\right] + \beta_4 \times \exp\left[1 - \left(\frac{P_s - P}{P_s}\right)^{\beta_5}\right] \tag{5}$$

where P stands for the pressure level, with the subscript s denoting the surface. β_j ($j = 1, 2, \ldots, 5$) are latitude-dependent parameters to be determined. Note the third term on the right-hand side of Equation 5 is
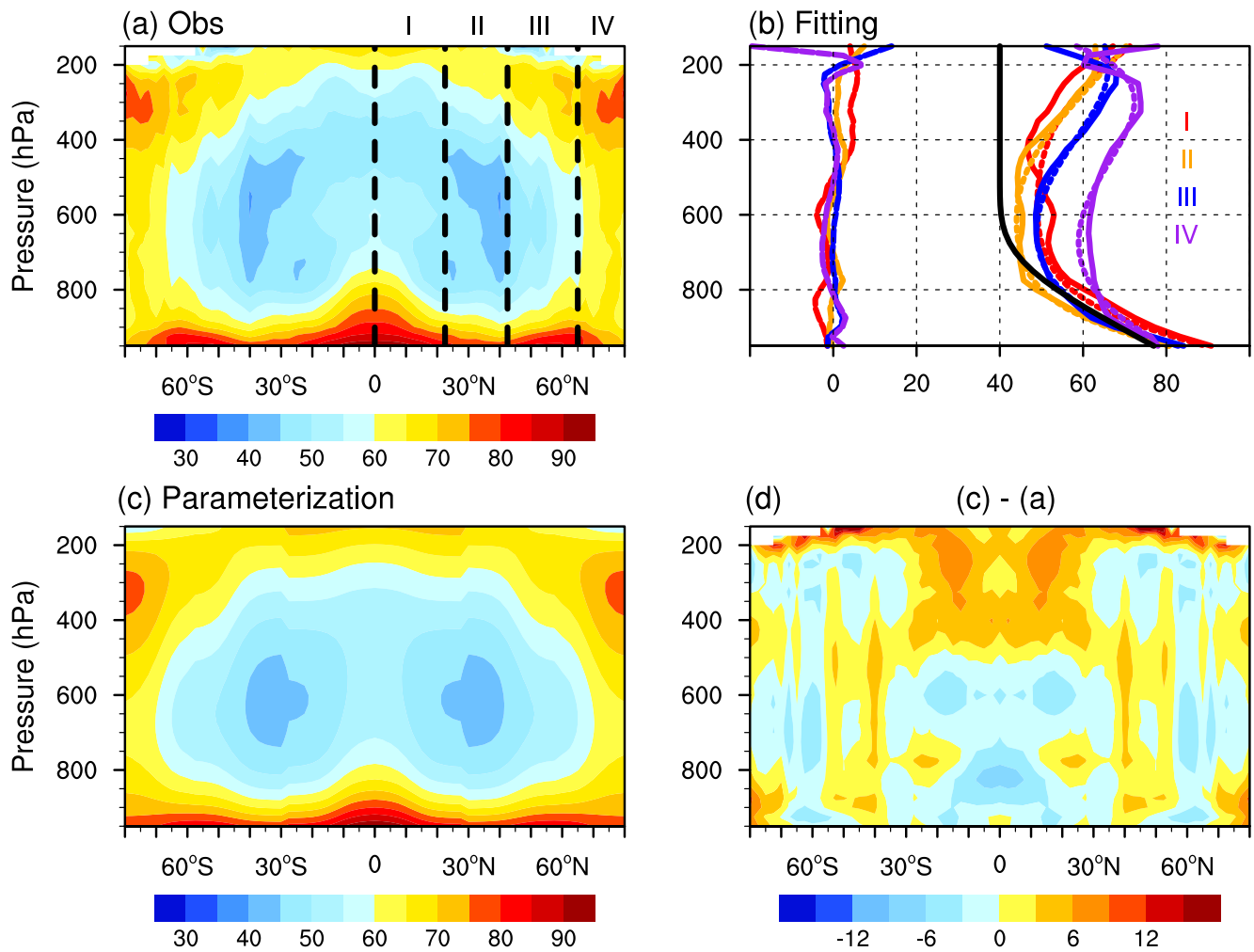
Figure 3. (a) Observed critical relative humidity (RH_c) (%) after symmetrization in the Northern Hemisphere and Southern Hemisphere. (b) Observed (dashed) and parameterized (solid) RH_c profiles in four representative regions, with the differences marked by long-dashed lines. The parameterized RH_c of Quaas (2012) is also superimposed in the figure (solid black) (c, d) Latitude–pressure cross-section of (c) the new parameterized RH_c and (d) its deviation against the observation.

introduced to allow RH_c to have a non-monotonic structure in the vertical. The coefficients β_j are determined by minimizing the cost function, as follows:

$$g = \sqrt{\frac{1}{N} \sum \left(\beta_1 + \beta_2 \times \exp\left[1 - \left(\frac{P}{P_s} \right)^{\beta_3} \right] + \beta_4 \times \exp\left[1 - \left(\frac{P_s - P}{P_s} \right)^{\beta_5} \right] - RH_c^{obs} \right)} \tag{6}$$

Table 1 lists the values of β_j in each latitudinal zone. Figure 3b shows the performance of the fitting. As can be seen, the fitting curves successfully capture the vertically varying structure as observed, with the bias mostly within the order of 2%. The relatively large bias near the TOA is most likely caused by a lack of sufficient samples at high levels. Figure 3b also superimposes the fitting of Q12, which underestimates RH_c by about 30% above 600 hPa compared to the observed values. The separated RH_c in each region is then combined into a single latitude-dependent formula in which the tangent function is used to make the parameterized RH_c vary smoothly at the edges of neighboring regions. The expression reads as

$$RH_c(\phi) = \frac{1 - \alpha_{idx(\phi)-1}}{2} RH_c(idx(\phi) - 1) + \frac{1 + \alpha_{idx(\phi)-1}}{2} RH_c(idx(\phi)) \tag{7}$$

where ϕ stands for latitude, and "idx" is the index of the region corresponding to latitude ϕ. $\alpha_{idx(\phi)}$ are weighing coefficients satisfying $\alpha_{idx(\phi)} = \tanh\left(\frac{\phi - \phi_o}{D_o} \right)$, where ϕ_0 and D_0 are tunable parameters, with their values shown in

Table 1
Coefficients Used in Critical Relative Humidity (RH$_c$) Fitting

Representative region	β_1	β_2	β_3	β_4	β_5
I ($|\phi| \leq 22.5°$)	137.4	−32.7	9.6	36.2	−3.3
II ($22.5° < \phi \leq 45°$)	130.4	−32.1	11.5	40.0	−1.9
III ($45° < |\phi| \leq 62.5°$)	−63.2	−133.2	−1.0	114.4	0.7
IV ($|\phi| > 62.5°$)	−79.1	−167.8	−1.1	−119.2	1.1
Latitude zone	ϕ_0	D_0			
$|\phi| \leq 30°$	10.0	6.5			
$30° < |\phi| \leq 60°$	48.0	6.5			
$|\phi| > 60°$	69.0	6.5			

Table 1. The performance of the full parameterization (NRH$_c$, hereafter) is shown in Figure 3c, which captures well the vertical and latitudinal varying structure as in CloudSat/CALIPSO. The fitting deviations shown in Figure 3d indicate that the biases are mostly within 5%, and the fitting in the lower troposphere generally has a higher accuracy than the fitting in the upper troposphere.

3. Model and Experiments

3.1. Model Introduction

The model used to investigate the impact of the new parameterized RH$_c$ on cloud simulation is FAMIL (Finite-volume Atmospheric Model of the IAP/LASG), which is an atmospheric component of the Chinese Academy of Sciences' coupled model, FGOALS (Flexible Global Ocean–Atmosphere–Land System Model). FAMIL uses a finite volume dynamical core on a cubed-sphere grid system (Bao et al., 2019; He et al., 2019; Li et al., 2019; Lin, 2004; Zhou et al., 2015), with the flux-form semi-Lagrangian scheme used for tracer advection (Lin & Rood, 1996; Wang et al., 2013). FAMIL is run at a resolution of roughly 1.9° latitude × 2.5° longitude, with 32 levels in the vertical and a time step of 1,800 s.

The physical parameterizations are basically the same as described in Zhou et al. (2015). The convection scheme originates from Tiedtke (1989), and was later modified by including variants of entrainment parameterization and closure assumption (Wang & Zhang, 2013, 2014). The Rapid Radiative Transfer Model for GCMs (RRTMG) is used for radiation computation (Clough et al., 2005), with cloud radiation computed based on samples drawn from a stochastic cloud generator (Wang et al., 2021). The boundary layer turbulent process is parameterized by a "non-local" first-order closure scheme that determines eddy diffusivity based on similarity theory (Holtslag & Boville, 1993). Cloud microphysics is represented by the single-moment scheme of Lin et al. (1983), which predicts bulk contents of cloud water, rain, snow, ice crystals, and graupel/hail. Fractional cloudiness is calculated according to a semi-empirical scheme that uses both relative humidity and cloud condensate as predictors (Xu & Randall, 1996a; hereafter XR96). In FAMIL, cloud condensate is formed at grid-scale saturation, while cloud fraction is represented at subgrid scales, which inevitably causes inconsistencies in the simulation of cloud fraction and cloud condensate. One purpose of this study is to remedy this problem by constructing an RH$_c$-based cloud scheme that calculates cloudiness and condensate synergistically.

3.2. Calculation of Subgrid-Scale Condensation

The subgrid-scale variability measured by RH$_c$ not only influences cloud fraction, but also cloud condensate formed during subgrid-scale condensation. Regarding the calculation of the latter, two different approaches are adopted, as described below.

3.2.1. Prognostic Method

This method retains the property of cloud condensate as a prognostic variable in models. Following Zhang et al. (2003), the prognostic equation for relative humidity U is expressed in terms of total water q_t, liquid water temperature T_l, and liquid water q_l:

$$\frac{\partial U}{\partial t} = \alpha \frac{\partial q_t}{\partial t} - \beta \frac{\partial T_l}{\partial t} - \gamma \frac{\partial q_l}{\partial t} \tag{8}$$

where $\alpha = \frac{1}{q_s}$, $\beta = \frac{q}{q_s^2} \frac{\partial q_s}{\partial T}$, and $\gamma = \alpha + \frac{L}{C_p} \beta$, with symbols q_s, C_p, L standing for the saturation specific humidity, the heat capacity at constant pressure, and the latent heat of vapourization, respectively. The saturation is calculated with respect to ice at temperatures below $-20°C$, and approximated by a linear weighted average of the saturation over ice and water in the $0°C$ to $-20°C$ temperature range. For the sake of simplicity, supersaturation for the ice process is not considered.

Noting $\frac{\partial U}{\partial t} = 0$ in the cloudy portion, together with the use of $\frac{\partial q_l}{\partial t} = C \frac{\partial \hat{q}_l}{\partial t} + c_m \hat{q}_l \frac{\partial C}{\partial t}$, Equation 8 is further expanded in the following form:

$$\left(1 + C \frac{L}{C_p} \frac{\partial q_s}{\partial T}\right) \frac{\partial \hat{q}_l}{\partial t} + c_m \hat{q}_l \frac{L}{C_p} \frac{\partial q_s}{\partial T} \frac{\partial C}{\partial t} = \frac{\partial \hat{q}_t}{\partial t} - \frac{\partial q_s}{\partial T} \frac{\partial T_l}{\partial t} \tag{9}$$

where a hat is used to denote variables in the cloudy portion of a grid box, C stands for cloud fraction, and c_m is the ratio of newly formed stratus to the pre-existing $\hat{q}_l$, setting as 0.1. By substituting $\frac{\partial C}{\partial t} = \frac{\partial C}{\partial U} \frac{\partial U}{\partial t}$ into Equation 8, one arrives at

$$\gamma C \frac{\partial \hat{q}_l}{\partial t} + \left[\left(\frac{\partial C}{\partial U}\right)^{-1} + \gamma c_m \hat{q}_l\right] \frac{\partial C}{\partial t} = \alpha \frac{\partial q_t}{\partial t} - \beta \frac{\partial T_l}{\partial t} \tag{10}$$

where $\frac{\partial C}{\partial U} = \frac{1}{2} \sqrt{\frac{1}{(1-U)(1-U_c)}}$, derived from Equation 1. Since q_t and T_l are conserved during the process of condensation, $\frac{\partial q_t}{\partial t}$ and $\frac{\partial T_l}{\partial t}$ can only be influenced by processes other than condensation, such as advection, convection, etc. Equations 9 and 10 thus form a closed set of equations to solve $\frac{\partial \hat{q}_l}{\partial t}$ and $\frac{\partial C}{\partial t}$. Recalling $\frac{\partial q_l}{\partial t} = C \frac{\partial \hat{q}_l}{\partial t} + c_m \hat{q}_l \frac{\partial C}{\partial t}$, the cloud condensate q_l can then be easily calculated. A caveat to this method is that the consistency between the updated cloudiness and condensate is not necessarily satisfied, because of the combined use of diagnostic cloudiness and prognostic condensate. Following Park et al. (2014), an additional adjustment is made to alleviate such inconsistencies in cases of "empty" or "dense" clouds.

3.2.2. Diagnostic Method Based on PDF

With a uniform PDF assumed for total water, one can also obtain a diagnostic formula for cloud condensate,

$$q_l = \int_{q_s}^{q_t + \Delta q} (q - q_s) \frac{1}{2\Delta q} \mathrm{d}q \tag{11}$$

which is further expanded as

$$q_l = \frac{(q_t + \Delta q)^2 - q_s^2}{4\Delta q} - \frac{1}{2\Delta q} (q_t + \Delta q - q_s).q_s \tag{12}$$

By expanding q_s in a Taylor's series, $q_s = q_{s,0} + \frac{\partial q_s}{\partial T} \frac{L}{C_p} (q_l - q_{l,0})$, with subscript "0" denoting the state before adjustment, q_l can be solved by using a Newton–Raphson iterative technique. Once q_l is obtained, the updated RH is then used in Equation 1 for cloudiness diagnosis. Calculating cloudiness and cloud condensate in this way ensures the consistency between cloud fraction and condensate, as both are derived from the same PDF.

Table 2
Experiment Descriptions

Experiment	Description	AMIP	APE
XR96	Cloud fraction calculated according to Xu and Randall (1996a)	✓	✗
Q12	Cloud fraction calculated according to Equation 1, with RH_c proposed by Quaas (2012)	✓	✓
Q12_pdf	Applying RH_c in both cloud cover and condensate, with the latter calculated using the PDF diagnostic method	✓	✓
Q12_prog	As in Q12_pdf but with the cloud condensate calculated using a prognostic method	✓	✓
NRHc	As in Q12 but using a new RH_c formula	✓	✓
NRHc_pdf	As in Q12_pdf but using a new RH_c formula	✓	✓
NRHc_prog	As in Q12_prog but using a new RH_c formula	✓	✓

3.3. Numerical Experiments

3.3.1. AMIP Experiment

The Atmospheric Model Intercomparison Project (AMIP)-type experiment forced by observed climatological sea surface temperature (SST) and sea ice is carried out to evaluate the performance of different cloud schemes in cloud simulation, including XR96 and the RH_c-based schemes with different RH_c formulae, that is, Q12 and NRH_c. Additional experiments are also carried out to investigate the impact of different techniques in dealing with subgrid-scale condensation. The suffixes "_pdf" and "_prog" represent the computation of subgrid-scale condensation using the PDF diagnostic method and the prognostic method, respectively. Descriptions of the experiments and their related abbreviations are given in Table 2. The model is integrated for 15 years for each experiment, with the output of the last 10 years used for analysis.

3.3.2. Aquaplanet Experiment

The analysis of cloud feedback is based on the aquaplanet experiment framework, in which the planet's surface is completely water-covered with fixed SST. Such settings suppress the interactions between the land surface, oceans and cryosphere, thus removing surface feedbacks in climate changes. Although the degree of model complexity is largely diminished in the aquaplanet framework, cloud feedbacks are found to be similar to those in their Earth-like configurations (Medeiros et al., 2008), the computational cost is dramatically decreased. To compare cloud feedbacks due to different RH_c configurations, we perform two sets of six simulations each: a control experiment using zonally symmetric SST, and a warmer experiment by uniformly increasing the SST by 4 K, analogous to a global warming scenario. Orbital parameters are set to perpetual equinox conditions with a fixed solar constant of 1,365 Wm^{-2}. Other forcings, such as gas and aerosol concentrations, are also zonally symmetric. For all simulations, the model is integrated for 5 years following the Aquaplanet Experiment Project (APE) protocol (Neale & Hoskins, 2000), with the output of the last 3 years used for analysis. Table 2 summarizes the cloud schemes used in the AMIP and aquaplanet experiments.

4. Comparisons of Cloud Simulation in AMIP Experiments

Figure 4 shows the global distribution of high-level ($p \leq 440$ hPa), mid-level ($440 < p \leq 680$ hPa), and low-level ($p > 680$ hPa) clouds simulated by different cloudiness schemes, along with CloudSat/CALIPSO satellite observations superimposed as a guiding reference. In experiments Q12 and NRH_c, the subgrid-scale condensation is switched off to prevent significant changes in the hydrological cycle, such that the differences in cloudiness can be mainly attributed to differences in the cloudiness formula. Observations show high-level clouds are mainly located in the Intertropical Convergence Zone (ITCZ), reaching as high as 80%, which is associated with massive detrainment of ice cumuli from deep convection. Active convection in the tropics also leads to a moderate amount of mid-level clouds, which accounts for about one-third of the high-level clouds. Low-level clouds are located along the storm tracks, in the middle-to-high latitudes of the Southern Hemisphere, and over the offshore of the eastern Pacific Ocean where subsidence prevails. Compared to CloudSat/CALIPSO, the XR96 scheme dramatically underestimates high- and mid-level clouds in the inner tropics, with the global mean value underestimated by up to 5.5% and 4.6%, respectively, which is partly due to a lack of parameterization for convective cloudiness
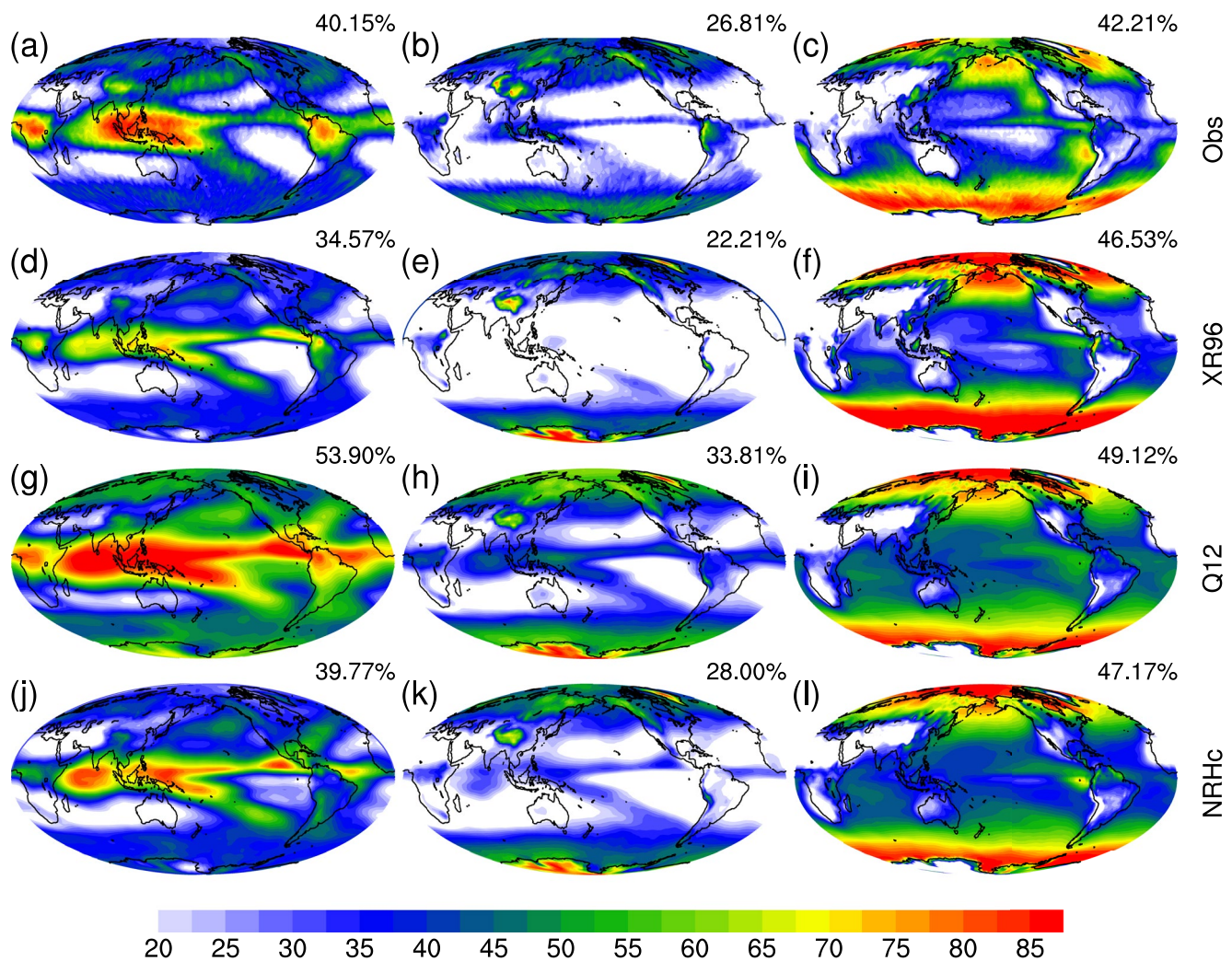
Figure 4. Geographical distribution of high (left column), mid (middle column) and low (right column) cloud cover (%) from (a–c) CloudSat/CALIPSO and simulations using the cloud scheme of (d–f) XR96 (g–i) Q12, and (j–l) NRH$_c$. The global mean value is shown in the top right of each figure.

in the model. On the other hand, it overestimates low-level clouds by 4.4%, with significant biases occurring in the polar regions, yet outperforms the RH$_c$-based schemes in terms of the global mean. When replaced with the RH$_c$-based schemes, the underestimations of high- and mid-level clouds are remarkably alleviated, which reproduce large occurrences of high cloud in the vicinity of the ITCZ. The bias sign changes from negative to positive in Q12, which conversely overestimates high- and mid-level clouds by about 13.8% and 7%, respectively. The overestimation of low-level clouds in the polar regions is reduced, but at the same time there are overestimations in the remaining regions, leading to an even worsened globally averaged result. The application of NRH$_c$ yields a better simulation than that of Q12, with the global mean bias within the order of 0.4%, 1.2%, and 4.9% for high-, mid- and low-level clouds, respectively, as opposed to 13.8%, 7%, and 6.9% in Q12 simulations. This demonstrates that while cloud fraction can be easily influenced by RH, the accuracy of RH$_c$ is also important in cloud simulation.

The biases in the vertically projected cloud cover can be traced back to biases in layer cloudiness. Figure 5 gives the zonally averaged vertical structure of cloud fraction for CloudSat/CALIPSO and the three simulations. Vertically continuous clouds in the deep tropics and shallow cumulus in the subtropics are evident in Cloud-Sat/CALIPSO, yet only marginally observed in XR96. These underestimations are mitigated in the RH$_c$-based scheme, which reproduces well the vertical cloud structure extending from the surface to 200 hPa in the tropics. Using a larger RH$_c$ as in NRH$_c$ produces fewer clouds than using a smaller RH$_c$ as in Q12—and this is further evidenced in Figure 6, which shows the difference in cloud amount depending on the choice of RH$_c$. This by itself
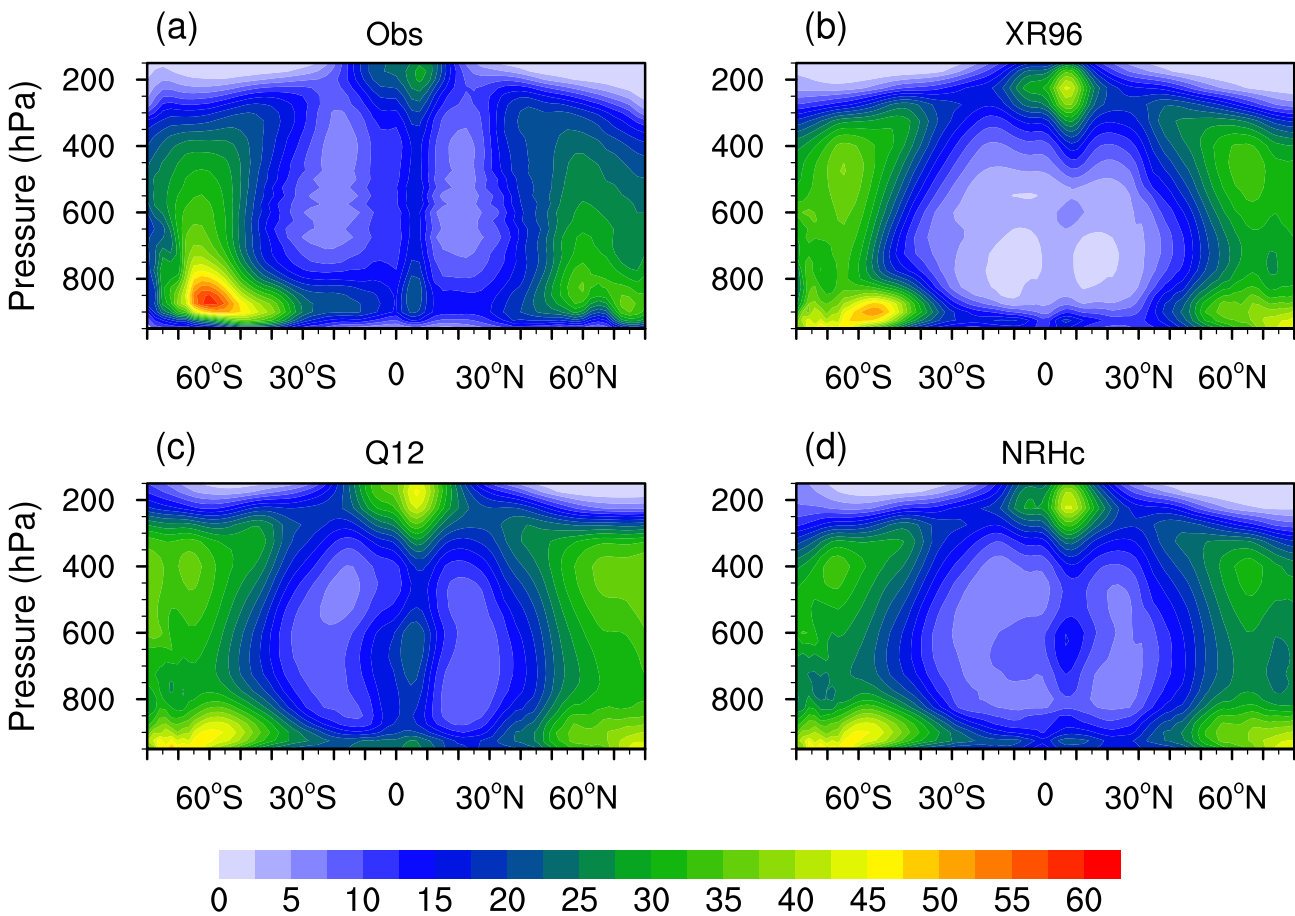
Figure 5. Latitude–pressure cross-section of the zonal mean cloud fraction (%) from (a) CloudSat/CALIPSO and simulations using the cloud scheme of (b) XR96, (c) Q12, and (d) NRH_c.

is trivial, since given the same relative humidity, increasing the RH_c increases the threshold for clouds to start forming, thus resulting in a lower occurrence of clouds. Similar phenomena are also observed in the simulations applying RH_c to both cloud cover and condensate (Figures 6b and 6c), although not as rigorously as in simulations applying RH_c to cloud cover alone. Different techniques for calculating subgrid-scale condensation lead to differences mainly in the upper layers. Moreover, the difference is more remarkable when comparing the simulations applying RH_c to cloud cover alone and those applying RH_c to both cloud cover and condensate. These differences may then translate into diversity and uncertainty in the cloud feedback, which is analyzed below.

5. Implications of RH_c for Cloud Feedback

5.1. Cloud Response to +4K SST

As RH_c is an important parameter in the cloud scheme, it is expected to influence the response of clouds to external forcings and thus the estimate of cloud feedback, which remains the greatest source of uncertainty in climate projections (Schneider et al., 2017; Zelinka et al., 2020). But to what extent can the range of cloud feedback uncertainty revealed in different models be attributed to the choice of RH_c and its implementation in a single model? A starting point for exploring this question is comparing the cloud response to +4K SST among different experiments, since most of the variation in cloud feedback arises from different cloud responses. Figure 7 shows the changes in zonally averaged cloud fraction and cloud liquid and ice water profiles for simulations applying different RH_c configurations listed in Table 2. An upward shift in clouds is observed in all simulations, extending across most of the troposphere at high altitudes and decreasing remarkably in layers below. Clouds respond in such a way so as to offset the effect of surface warming, following the fixed anvil temperature hypothesis
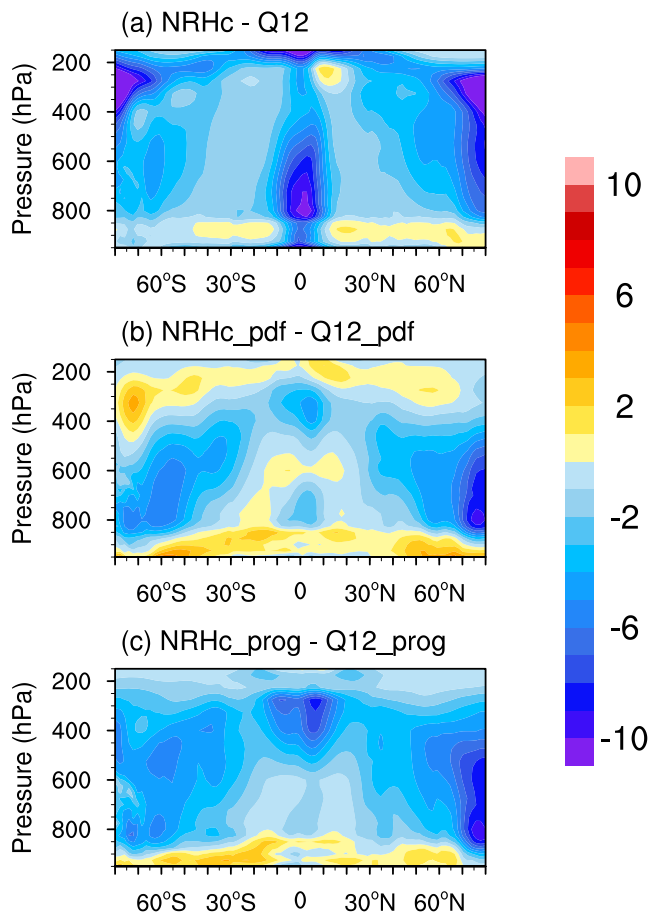
Figure 6. Differences in cloud fraction (%) between the critical relative humidity (RH_c) choice of NRH_c and Q12 in simulations (a) applying RH_c only in cloud cover, and (b, c) applying RH_c in both cloud cover and cloud condensate, with the subgrid-scale condensation calculated using the PDF (b) diagnostic and (c) prognostic method.

(Hartmann & Larson, 2002). This is accompanied by elevated cloud ice (right column), which is caused by enhanced deep convection in the tropics that detrains cloud ice crystals at high altitudes. While all simulations are common in producing such features, the models show obvious discrepancies in the magnitude of the response. For simulations applying the prognostic approach in calculating subgrid-scale condensation (Figure 7i and 7r), the changes in cloud ice are more pronounced than those in the remaining simulations, regardless of the choice in RH_c. Another striking feature is the different response of cloud liquid water. While most simulations produce an increase in cloud liquid water in the polar regions (poleward of 60°) and a decrease in the subtropics, Q12_prog produces a consistent increase across all latitudes (Figure 7h). The sensitivity of cloud condensate to RH_c is larger in simulations applying RH_c in both cloud cover and condensate than those applying RH_c in cloud cover alone, suggesting the role of RH_c in regulating climate is limited in the latter. There are also noticeable differences due to different approaches dealing with subgrid-scale condensation, which are comparable or even larger than those caused by the choice in RH_c. This implies that the diversity of cloud feedback may arise from different techniques in the implementation of RH_c, in addition to the variation in RH_c itself.

Figure 8 shows histograms of changes in global-mean cloud fraction viewed by the International Satellite Cloud Climatology Project (ISCCP) simulator, which partitions clouds into cloud top pressure (CTP) and optical depth (τ) bins. Viewing clouds in this manner facilitates the computation of cloud feedback using the cloud radiative kernel technique (Zelinka et al., 2012). All simulations consistently show a reduction in global-averaged cloudiness, ranging from 1.3% to 6.1%. A robust decrease occurs in low-topped clouds, accompanied by a modest increase in high-topped clouds. This is in accordance with increased cloudiness at high altitudes and decreased cloudiness at low latitudes (Figure 7). When stratified in the τ range, clouds tend to shift from optically medium bins to thick ones, which is more evident in simulations applying RH_c in both cloud cover and condensate. By comparing the two rows, we can see that the sensitivity to RH_c is smaller in simulations applying RH_c in cloud cover alone than those applying it in both cloud cover and condensate, in agreement with the findings of Figure 7. Results are also sensitive to the manner how subgrid-scale condensation is calculated, with the PDF diagnostic approach producing more pronounced changes in some of the cloud regimes than the prognostic approach.

We further partition clouds into different categories. In the left column of Figure 9, we show changes in the occurrence of thick ($\tau > 23$), medium ($3.6 < \tau \leq 23$) and thin ($\tau \leq 3.6$) clouds in simulations applying NRH_c in the cloud scheme, along with the differences against simulations applying Q12 in the right column. All three simulations show an increase in thick clouds and a decrease in thin clouds poleward of 60°, with the magnitude varying considerably between each other. Note that for display purpose, the green curves in the left column use the right ordinate. Altering RH_c in each experiment leads to differences mainly in the polar regions, and to a lesser degree in the tropics and subtropics. However, even small differences in cloud changes at low latitudes can lead to large differences in shortwave (SW) cloud feedback, because the SW kernel reaches its maximum at the equator.

Figure 10 shows the changes in cloud fraction stratified according to cloud top height. The changes are overall positive for high-topped ($p \leq 440$ hPa) clouds and negative for low-topped ($p > 680$ hPa) clouds in all three simulations applying NRH_c in the cloud scheme. The mid-topped ($440 < p \leq 680$ hPa) clouds generally increase poleward of 60° and decrease between 30° and 60°. These behaviors can be coarsely inferred from the layer cloudiness shown in Figure 7, although the definition of cloud top height differs between the simulator and models (Bodas-Salcedo et al., 2011; Wang, 2022a). In contrast to the apparent differences found by partitioning clouds according to τ, the curves are close to each other in most regions except for low-topped clouds in the
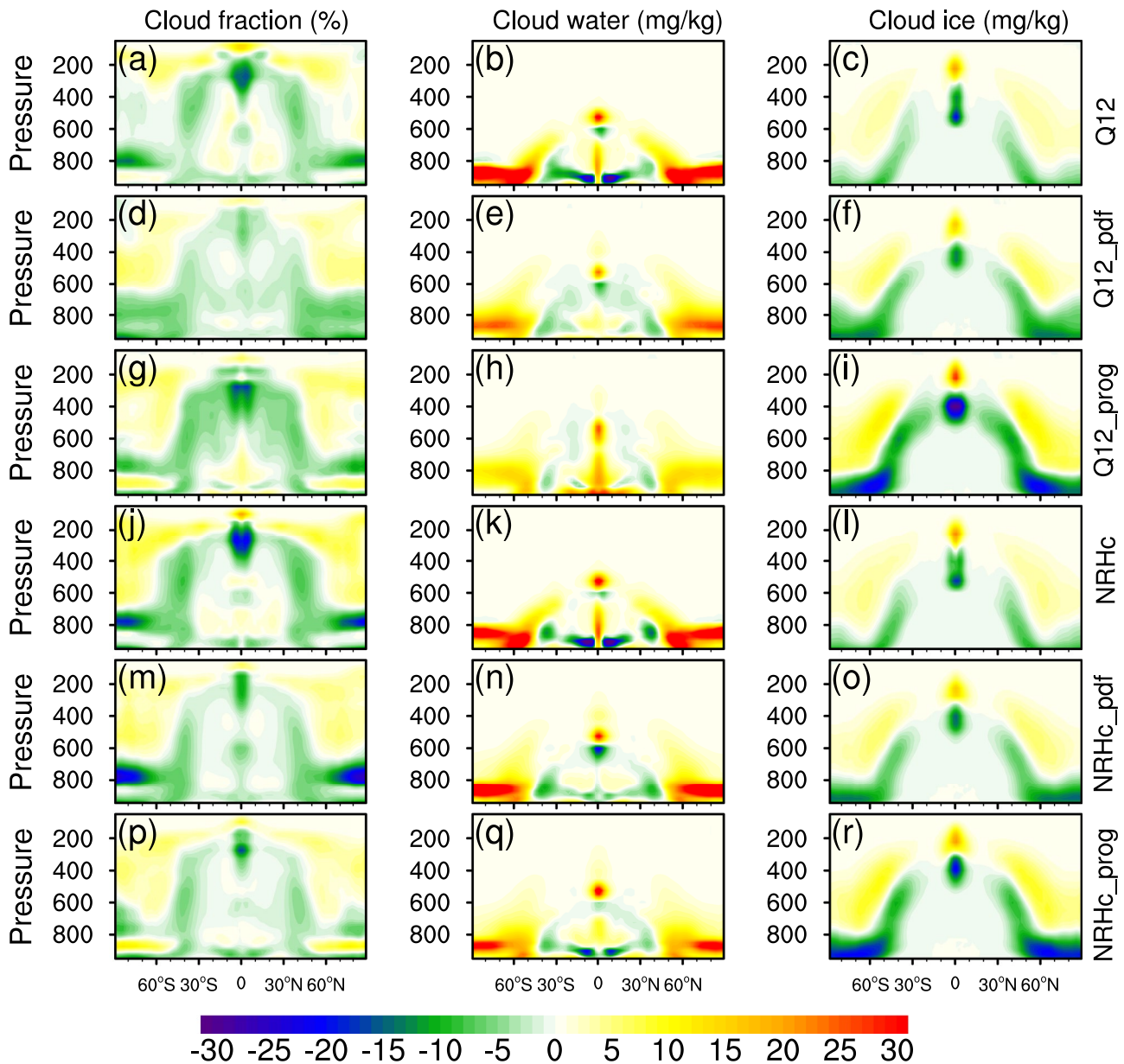
Figure 7. Changes in cloud fraction (%, left column), cloud liquid water (mg kg^{-1}, middle column), and cloud ice water (mg kg^{-1}, right column) between the +4 K and control experiments in simulations with different critical relative humidity (RH$_c$) configurations.

extratropics. The reason is that subgrid-scale condensation mainly affects the concentration of cloud condensate but barely influences the cloud vertical structure, which is more relevant to the determination of cloud top height. This would imply a smaller diversity in longwave (LW) cloud feedback than for SW cloud feedback, since the former is mainly influenced by high-topped clouds while the latter is more affected by optically thick clouds. Regarding the sensitivity to RH$_c$, the difference is more remarkable in simulations calculating subgrid-scale condensation using the prognostic approach (red curve). Given the overall consistency between each curve in the left panel, the apparently large differences in the right panel reflect large differences arising from a smaller choice of RH$_c$. This can be caused by a combination of the following two reasons: (a) As Q12 is systematically smaller than NRH$_c$, the completely clear skies in NRH$_c$ simulations now become partially cloudy skies; (b) The more frequent interaction between cloud macrophysics and other parts in the model increases the diversity of model behavior.
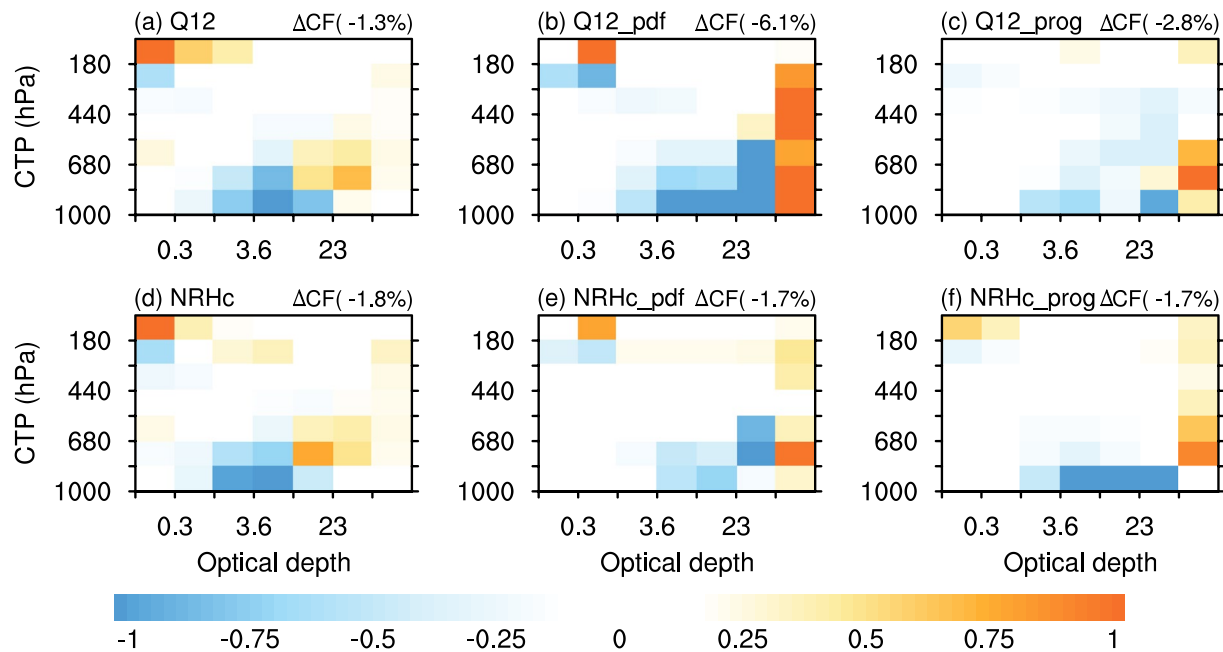
Figure 8. Globally averaged changes in cloud fraction in CTP-τ histograms between the +4 K and control experiments in simulations with different critical relative humidity (RH$_c$) configurations. The sum of each matrix is shown in the top right of each panel.
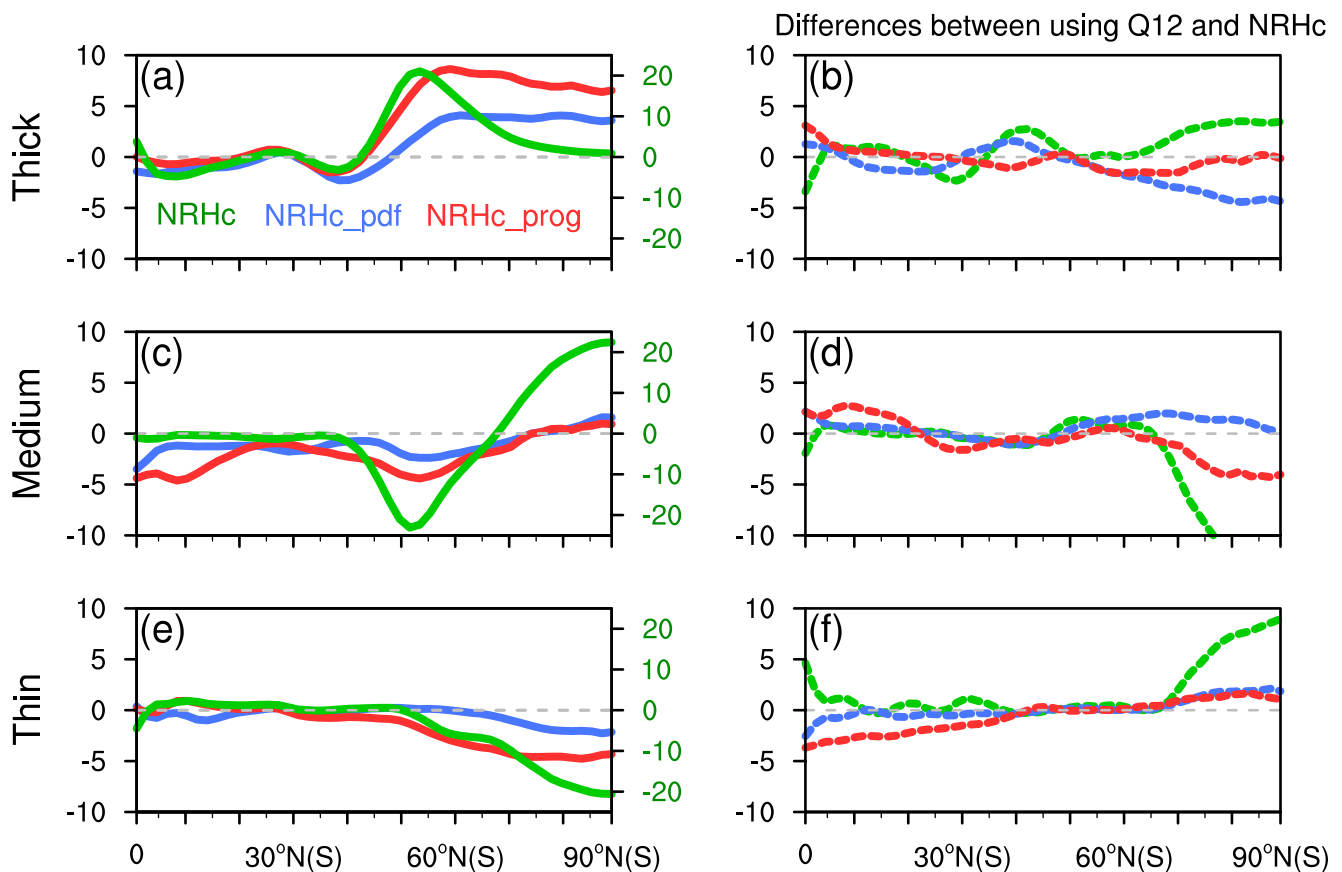

Figure 9. Changes in the occurrence of thick ($\tau > 23$), medium ($3.6 < \tau \leq 23$), and thin ($\tau \leq 3.6$) clouds in simulations with NRH$_c$ applied in the cloud scheme (left column), and the differences against simulations with Q12 applied (right column). In the left column, green curves in the left column use the right ordinate. Units: %.
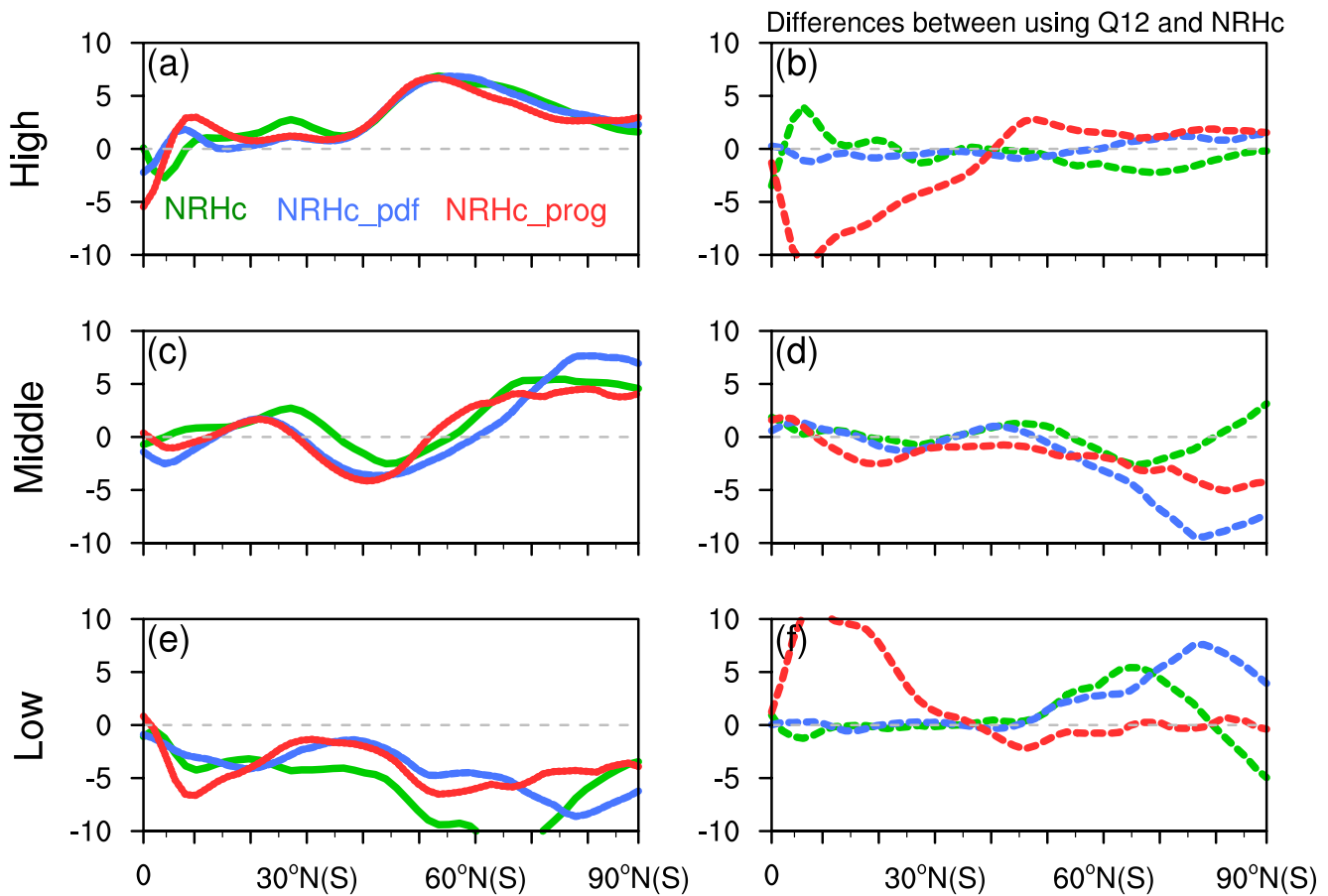
Figure 10. Changes in the occurrence of high-topped ($p \leq 440$ hPa), mid-topped ($440 < p \leq 680$ hPa), and low-topped ($p > 680$ hPa) clouds in simulations with NRH_c applied in the cloud scheme (left column), and the differences against simulations with Q12 applied (right column). Units: %.

5.2. Cloud Feedback Analysis

Figure 11 presents the zonally averaged SW, LW, and net cloud feedback calculated using cloud radiative kernels. Details for the kernel technique and comparisons with other approaches are given in Appendix A. The LW cloud feedback is positive at all latitudes except at the equator, with the pattens closely resembling those of high-cloud changes (Figure 10a). This is because the LW kernel increases strongly with decreasing CTP, and thus the LW cloud feedback is mostly determined by changes in high-topped clouds. On the other hand, SW cloud feedback is relevant to cloud changes at all altitudes, and the impact is more sensitive to cloud optical depth, as well as the condition of solar zenith. Because SW kernel maximizes at the equator, large discrepancies in cloud feedback are observed in these regions despite small cloudiness changes. The agreement between each curve on the cloud feedback of LW is better than that of SW. Because SW cloud feedback dominates over LW cloud feedback at most latitudes, the patterns of net cloud feedback resemble those of SW cloud feedback. Altering RH_c leads to differences mainly at low latitudes, exceeding 2 Wm^{-2}K^{-1} for both SW and LW cloud feedback. The differences between each curve are larger than those in the left panel, implying the use of smaller RH_c tends to broaden the diversity of cloud feedback.

To explore cloud feedback contributed by different cloud types, Figure 12 shows the global-mean cloud feedback partitioned by high, middle, low, thin, medium, and thick clouds. Considerable spread is evident in the SW cloud feedback, especially for low- and high-topped clouds, spanning a wide range of about 2 Wm^{-2}K^{-1}. The diversity of LW cloud feedback is relatively smaller than that of SW, with the largest spread occurring in high-topped clouds reaching 1 Wm^{-2}K^{-1}. Using smaller RH_c leads to larger spread than using larger ones, in line with the assertion previously made. For each cloud type, the anticorrelation between LW and SW cloud feedback results in reduced diversity of the net cloud feedback. The largest spread occurs in low clouds because of the exceptional
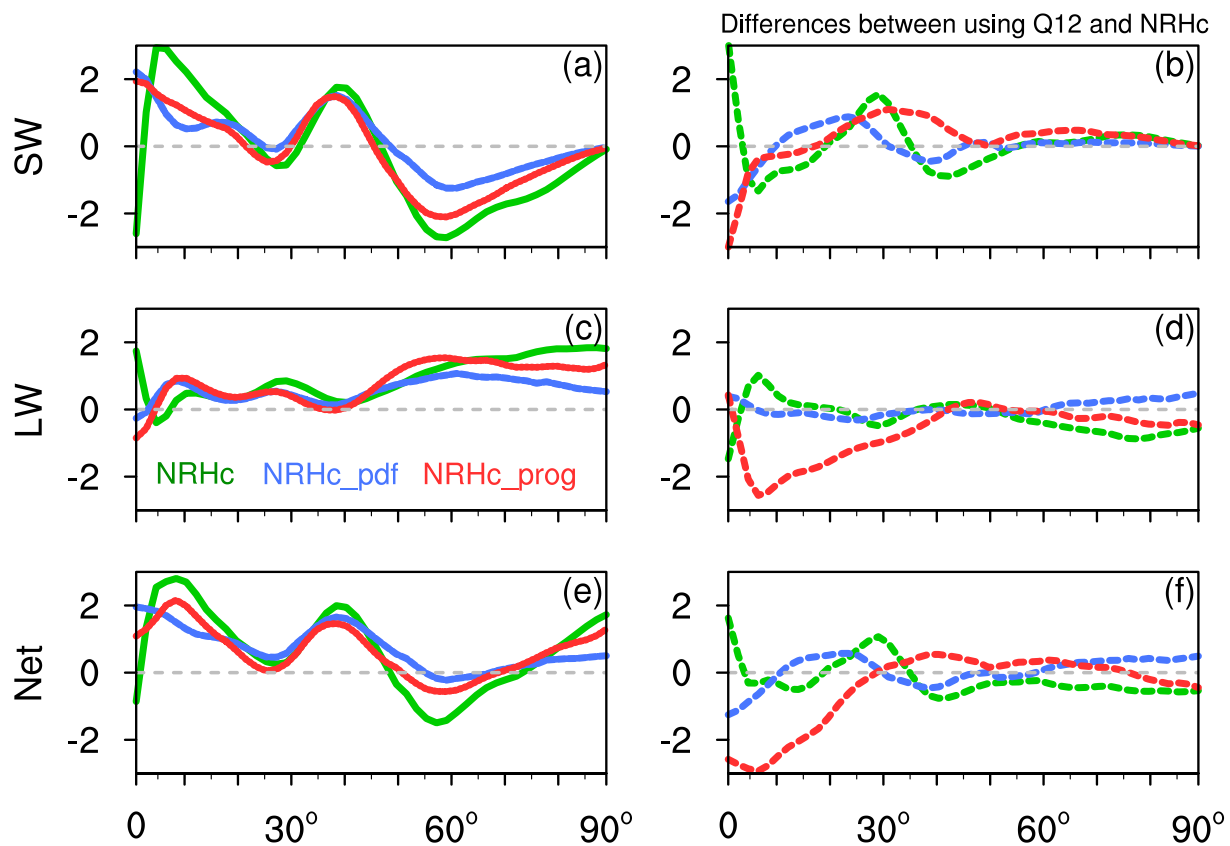
Figure 11. Zonally averaged SW, LW and net cloud feedback calculated using cloud radiative kernels in simulations with NRH$_c$ applied in the cloud scheme (left column), and the differences against simulations with Q12 applied (right column). Units: Wm^{-2}K^{-1}.

value in Q12_prog, and to a lesser degree in optically thick clouds. While many previous studies (e.g., Bony & Dufresne, 2005; Cesana et al., 2017; Zelinka et al., 2012) have emphasized the diversity of cloud feedback due to low clouds, varying RH$_c$ and its implementation leads to the diversity of cloud feedback mainly arising from optically thick clouds.

Figure 13 shows the global-mean cloud feedbacks for different simulations estimated by three different methods— the cloud radiative kernel technique (Zelinka et al., 2012), adjusting ΔCRE by considering cloud masking effects (Shell et al., 2008; Soden et al., 2008), and directly using ΔCRE to diagnose cloud feedback (Cess & Potter, 1988). Also shown are multimodel cloud feedbacks estimated by ΔCRE from the CMIP6 APE experiments. The ΔCRE method systematically leads to larger cloud feedbacks for SW and smaller ones for LW in comparison with the other two. Although the ΔCRE method is not a rigorous estimate of realistic cloud–climate feedbacks, it provides an indication of diversity in models. It is found that the range of net cloud feedback uncertainty in different models is nearly replicated by varying RH$_c$ and the techniques in calculating subgrid-scale condensation in a single model. Even after excluding Q12_prog, the spread reaches 40% of that found in multiple models. This highlights the importance of RH$_c$ and its implementation in models in inducing cloud feedback diversity. It is also apparent that the spread caused by different treatment of subgrid-scale condensation is larger than that caused by the choice of RH$_c$.

6. Summary and Conclusions

This study investigates the RH$_c$ diagnosed from CloudSat/CALIPSO, which is approximately a measure of subgrid-scale variability of moisture. The observed RH$_c$ exhibits distinct geographical distributions, with relatively low values in the subtropics and high values in the polar regions. Also found is a non-monotonic vertical structure that decreases from the surface to the mid-levels and then increases in upper layers. A globally uniform, vertically monotonically varying profile of RH$_c$ as parameterized in many studies (e.g., Sundqvist
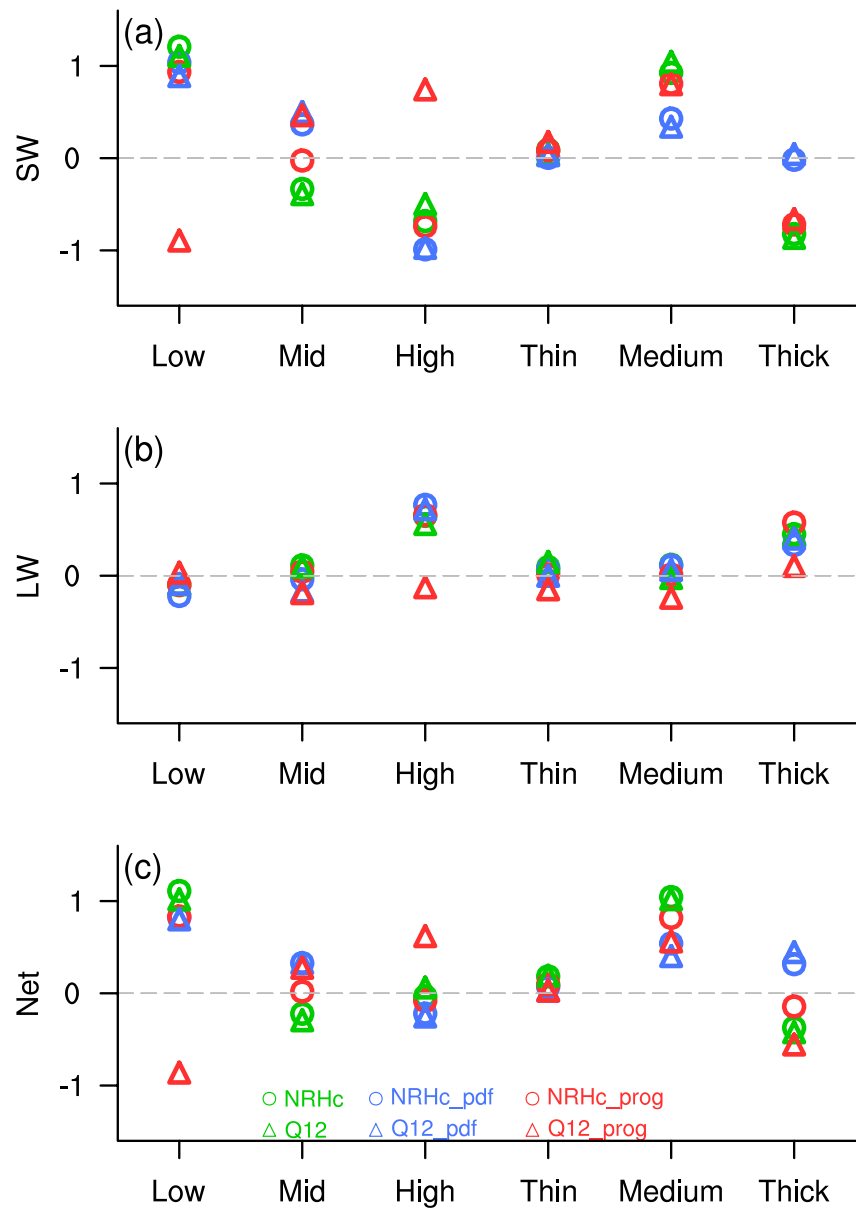
Figure 12. Global- and annual-mean (a) SW cloud feedback, (b) longwave (LW) cloud feedback, and (c) net cloud feedback, partitioned by high, middle, low, thin, medium, and thick clouds in simulations with different critical relative humidity (RH$_c$) configurations. Units: Wm^{-2}K^{-1}.

et al., 1989; Q12) thus fails to capture the observed RH$_c$ with sufficient accuracy. An improved formula for RH$_c$ is addressed by incorporating latitudinal dependence and the bimodal structure in the vertical, which successfully captures the vertical and latitudinal variations as in CloudSat/CALIPSO, with the bias mostly within 5%. Although the RH$_c$ formula is climatologically based, different from the time-varying characteristics pursued by process-oriented parameterizations, it serves as a guiding reference for the time-averaged subgrid-scale variability in parameterizations.

With the parameterized RH$_c$, a cloud macrophysics scheme is constructed in which fractional cloudiness and subgrid-scale condensation are synergistically solved, in contrast to the default XR96 scheme used in FAMIL that calculates cloud fraction only. The AMIP-type experiment is then conducted to evaluate the performance of different schemes on cloud simulation, including XR96, Q12, and NRH$_c$. Results show that the RH$_c$-based schemes largely alleviate the underestimation of high- and mid-level clouds in the default model, while better simulation
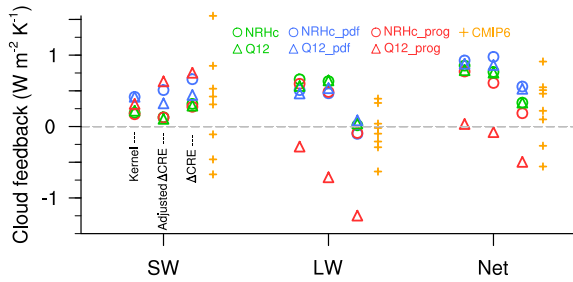
Figure 13. Global- and annual-mean cloud feedbacks estimated by three different methods in simulations with different critical relative humidity (RH_c) configurations. The multimodel cloud feedbacks estimated by ΔCRE from the CMIP6 APE experiments are also overlaid, with each model represented by a plus sign.

of low-level clouds are produced by XR96. The application of NRH_c yields better simulations than Q12, with the global-mean bias within the order of 0.4%, 1.2%, and 4.9% for high-, mid- and low-level clouds, respectively, as opposed to 13.8%, 7%, and 6.9% in Q12 simulations. This demonstrates the importance of the accuracy of RH_c in cloud simulation. The larger occurrence of clouds in Q12 is in accordance with its smaller magnitude, which decreases the threshold for clouds to start forming. Similar phenomena are also observed in simulations applying RH_c to both cloud cover and condensate, yet the pattens are different among the simulations. These differences may then easily transfer into the diversity and uncertainty of cloud feedback.

Control and +4K SST aquaplanet experiments are carried out to investigate the sensitivity of cloud feedback to RH_c and its implementation. While all simulations commonly produce an upward shift feature of clouds in response to +4K warming, the modeled clouds show obvious discrepancies in the magnitude of the response. The sensitivity of cloud changes to RH_c is larger in simulations applying RH_c in both cloud cover and condensate than those applying it in cloud cover alone, because in the former the hydrological feedback between cloud macrophysics and other parts in the model increases the diversity of model behavior. For the same reason, using a smaller RH_c tends to produce greater sensitivity than using a larger one.

While many previous studies have emphasized the diversity in cloud feedback due to low clouds, varying RH_c and its implementation leads to the diversity of cloud feedback being mainly due to optically thick clouds. Using smaller RH_c values leads to larger spread than using larger ones. Furthermore, the spread caused by different treatments of subgrid-scale condensation is larger than that caused by the choice of RH_c. A large portion of cloud feedback diversity in different CMIP6 models is replicated by varying RH_c and its implementation in a single model, highlighting the importance of RH_c in inducing cloud feedback diversity.

Appendix A: Methodology for Cloud Feedback Estimation

Following Zelinka et al. (2012), multiplying the change in cloud fraction for each ISCCP cloud type by the corresponding cloud radiative kernel yields an estimate of the contribution of each cloud type to the change in radiation at the TOA:

$$\Delta R_{cloud}\left(\text{lon}, \text{lat}, P_{top}, \tau\right) = \frac{\partial R}{\partial C\left(P_{top}, \tau\right)} \times \Delta C\left(\text{lon}, \text{lat}, P_{top}, \tau\right) \tag{A1}$$

where $\Delta R_{cloud}(\text{lon}, \text{lat}, P_{top}, \tau)$ is the contribution to the TOA flux anomaly from the cloud fraction anomaly at a particular location and for clouds with a particular P_{top} and τ [$\Delta C(\text{lon}, \text{lat}, P_{top}, \tau)$]. The term $\frac{\partial R}{\partial C(P_{top}, \tau)}$ represents the cloud radiative kernel, which is calculated using RRTMG with atmospheric and surface conditions derived from the control aquaplanet climate. Cloud feedback is then obtained by summarizing the contribution of all cloud types normalized by the change in global-mean surface temperature (i.e., 4 K). This method overcomes the invalidity of using radiative kernels to estimate cloud feedback owing to strong nonlinearities of TOA flux to cloud amount perturbations. Besides, it allows one to attribute the contributions of specific cloud types to cloud feedback, thus casting useful physical light on its causes.

Another approach to estimate ΔR_{cloud} is by subtracting the cloud masking effects of changing temperature, water vapor, surface albedo and radiative forcing from the change in the cloud radiative effect (CRE) (Shell et al., 2008; Soden et al., 2008):

$$\Delta R_{cloud} = \Delta CRE + \left(K_T^0 - K_T\right) dT + \left(K_q^0 - K_q\right) dq \tag{A2}$$

where K_T and K_q are radiative kernels for temperature and water vapor calculated using RRTMG, with superscript "0" denoting the clear sky. In Equation A2, the cloud masking effects due to the forcing change and albedo feedback have been dropped as their responses to global warming are suppressed in the aquaplanet framework.

Figure A1 shows a scatterplot of cloud feedbacks calculated using cloud radiative kernels versus those calculated by adjusting ΔCRE. Each point represents the feedback computed for a single month at a single location in the model. For both SW and LW cloud feedbacks, the points collapse reasonably well on a line, with the correlation coefficients exceeding 0.8 for SW and 0.9 for LW. The regression slopes lie mostly within 10% of the one-to-one line for LW (except for Q12_pdf and Q12_prog) and within 20% for SW (except for Q12_pdf, Q12_prog and NRHc_pdf). The poor agreement for SW might presumably be caused by the overly coarse resolution of τ in SW cloud radiative kernels, which is more sensitive to changes in τ.
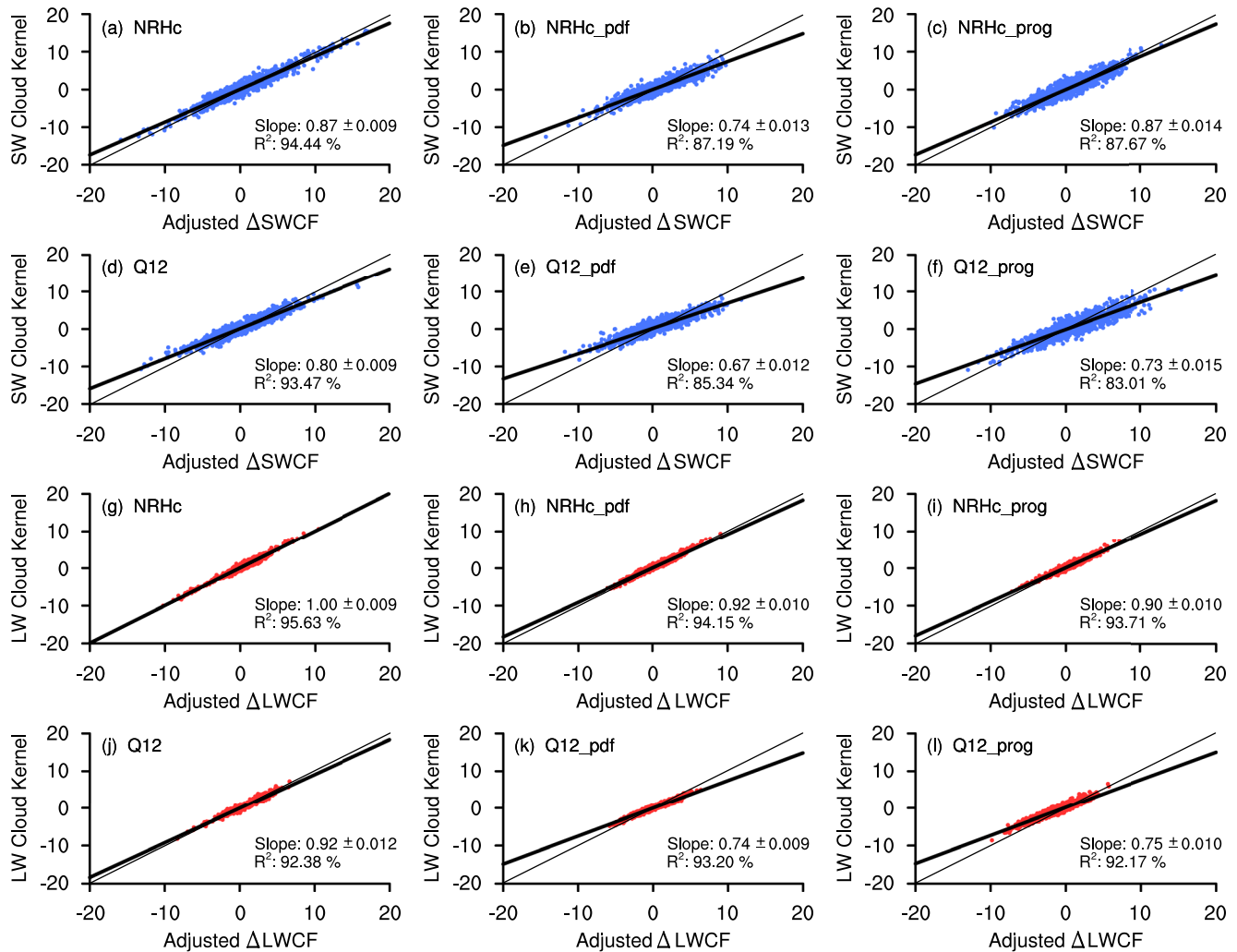

Figure A1. Scatterplot of (a–f) SW–cloud feedback and (g–l) LW–cloud feedback estimated between using the method of adjusting ΔCRE by considering cloud masking effects and the cloud radiative kernel method. The thin line is the one-to-one line, and the thick line is the linear least squares fit to the data. The slope and 2σ range of uncertainty of this regression line along with the fraction of variance explained by the fit are provided in each panel. Units: $Wm^{-2}K^{-1}$.

Data Availability Statement

The CloudSat/CALIPSO data products are accessible through the CloudSat Data Processing Center website at https://www.cloudsat.cira.colostate.edu/. The ECMWF-AUX product is available at https://www.cloudsat.cira.colostate.edu/data-products/ecmwf-aux. The source code of the FAMIL model can be downloaded from http://doi.org/10.5281/zenodo.4588109 (Li, 2021). The aquaplanet radiative kernels are available for download at https://doi.org/10.5281/zenodo.6381831 (Wang, 2022b).

References

Bao, Q., Wu, X., Li, J., Wang, L., He, B., Wang, X., et al. (2019). Outlook for el Niño and the Indian ocean dipole in autumn-winter 2018–2019 (in Chinese). *Chinese Science Bulletin*, *64*(1), 73–78. https://doi.org/10.1360/N972018-00913

Barker, H. W. (2008). Overlap of fractional cloud for radiation calcula-tions in GCMs: A global analysis using CloudSat and CALIPSO data. *Journal of Geophysical Research*, *113*, D00A01. https://doi.org/10.1029/2007jd009677

Bodas-Salcedo, A., Webb, M., Bony, S., Chepfer, H., Dufresne, J.-L., Klein, S., et al. (2011). COSP: Satellite simulation software for model assessment. *Bulletin of the American Meteorological Society*, *92*(8), 1023–1043. https://doi.org/10.1175/2011BAMS2856.1

Bony, S., & Dufresne, J.-L. (2005). Marine boundary layer clouds at the heart of tropical cloud feedback uncertainties in climate models. *Geophysical Research Letters*, *32*(20), L20806. https://doi.org/10.1029/2005GL023851

Bony, S., & Emanuel, K. (2001). A parameterization of the cloudiness associated with cumulus convection; evaluation using TOGA COARE data. *Journal of the Atmospheric Sciences*, *58*(21), 3158–3183. https://doi.org/10.1175/1520-0469(2001)058<3158:APOTCA>2.0.CO;2

Cesana, G., Suselj, K., & Brient, F. (2017). On the dependence of cloud feedbacks on physical parameterizations in WRF aquaplanet simulations. *Geophysical Research Letters*, *44*(20), 10762–10771. https://doi.org/10.1002/2017GL074820

Cess, R., & Potter, G. (1988). A methodology for understanding and intercomparing atmospheric climate feedback processes in general circula-tion models. *Journal of Geophysical Research*, *93*(D7), 8305–8314. https://doi.org/10.1029/JD093iD07p08305

Cheng, A., & Xu, K.-M. (2006). Simulation of shallow cumuli and their transition to deep convective clouds by cloud-resolving models with different third-order turbulence closures. *Quarterly Journal of the Royal Meteorological Society*, *132*(615), 359–382. https://doi.org/10.1256/qj.05.29

Cheng, A., & Xu, K.-M. (2015). Improved low-cloud simulation from the Community Atmosphere Model with an advanced third-order turbu-lence closure. *Journal of Climate*, *28*(14), 5737–5762. https://doi.org/10.1175/JCLI-D-14-00776.1

Clough, S., Shephard, M., Mlawer, E., Delamere, J., Iacono, M., Cady-Pereira, K., et al. (2005). Atmospheric radiative transfer modeling: A summary of the AER codes. *Journal of Quantitative Spectroscopy and Radiative Transfer*, *91*(2), 233–244. https://doi.org/10.1016/j.jqsrt.2004.05.058

Fetzer, E., Read, W., Waliser, D., Kahn, B., Tian, B., Vömel, H., et al. (2008). Comparison of upper tropospheric water vapor observations from the microwave limb sounder and atmospheric infrared sounder. *Journal of Geophysical Research*, *113*(D22), D22110. https://doi.org/10.1029/2008JD010000

Golaz, J.-C., Larson, V., & Cotton, W. (2002). A PDF-based model for boundary layer clouds. Part I: Method and model description. *Journal of the Atmospheric Sciences*, *59*(24), 3540–3551. https://doi.org/10.1175/1520-0469(2002)059<3540:APBMFB>2.0.CO;2

Hartmann, D., & Larson, K. (2002). An important constraint on tropical cloud—climate feedback. *Geophysical Research Letters*, *29*(20), 1951. https://doi.org/10.1029/2002GL015835

He, B., Bao, Q., Wang, X., Zhou, L., Wu, X., Liu, Y., et al. (2019). CAS FGOALS-f3-L model datasets for CMIP6 historical Atmospheric Model Intercomparison Project simulation. *Advances in Atmospheric Sciences*, *36*(8), 771–778. https://doi.org/10.1007/s00376-019-9027-8

Holtslag, A., & Boville, B. (1993). Local versus nonlocal boundary-layer diffusion in a global climate model. *Journal of Climate*, *6*(10), 1825–1842. https://doi.org/10.1175/1520-0442(1993)006<1825:LVNBLD>2.0.CO;2

Kahn, B., & Teixeira, J. (2009). A global climatology of temperature and water vapor variance scaling from the atmospheric infrared sounder. *Journal of Climate*, *22*(20), 5558–5576. https://doi.org/10.1175/2009JCLI2934.1

Larson, V., Schanen, D., Wang, M., Ovchinnikov, M., & Ghan, S. (2012). PDF parameterization of boundary layer clouds in models with horizon-tal grid spacings from 2 to 16 km. *Monthly Weather Review*, *140*(1), 285–306. https://doi.org/10.1175/mwr-d-10-05059.1

Li, J. (2021). The code of FGOALS-f3 [Computer software]. Zenodo. https://doi.org/10.5281/zenodo.4588109

Li, J., Bao, Q., Liu, Y., Wu, G., Wang, L., He, B., et al. (2019). Evaluation of FAMIL2 in simulating the climatology and seasonal-to-in-terannual variability of tropical cyclone characteristics. *Journal of Advances in Modeling Earth Systems*, *11*(4), 1117–1136. https://doi.org/10.1029/2018MS001506

Lin, S.-J. (2004). A "vertically Lagrangian" finite-volume dynamical core for global models. *Monthly Weather Review*, *132*(10), 2293–2307. https://doi.org/10.1175/1520-0493(2004)132<2293:AVLFDC>2.0.CO;2

Lin, S.-J., & Rood, R. (1996). Multidimensional flux-form semi-Lagrangian transport schemes. *Monthly Weather Review*, *124*(9), 2046–2070. https://doi.org/10.1175/1520-0493(1996)124<2046:MFFSLT>2.0.CO;2

Lin, Y. (2014). Humidity variability revealed by a sounding array and its implications for cloud representation in GCMs. *Journal of Geophysical Research: Atmospheres*, *119*(17), 10499–10514. https://doi.org/10.1002/2014JD021837

Lin, Y.-L., Farley, R., & Orville, H. (1983). Bulk parameterization of the snow field in a cloud model. *Journal of Applied Meteorology*, *22*(6), 1065–1092. https://doi.org/10.1175/1520-0450(1983)022<1065:BPOTSF>2.0.CO;2

Medeiros, B., Stevens, B., Held, I., Zhao, M., Williamson, D., Olson, J. G., & Bretherton, C. S. (2008). Aquaplanets, climate sensitivity, and low clouds. *Journal of Climate*, *21*(19), 4974–4991. https://doi.org/10.1175/2008JCLI1995.1

Miao, H., Wang, X., Liu, Y., & Wu, G. (2019). An evaluation of cloud vertical structure in three reanalyses against CloudSat/cloud-aerosol lidar and infrared pathfinder satellite observations. *Atmospheric Science Letters*, *20*(7), e906. https://doi.org/10.1002/asl.906

Neale, R., & Hoskins, B. (2000). A standard test for AGCMs including their physical parametrizations: I: The proposal. *Atmospheric Science Letters*, *1*(2), 101–107. https://doi.org/10.1006/asle.2000.0022

Neggers, R. (2009). A dual mass flux framework for boundary layer convection. Part II: Clouds. *Journal of the Atmospheric Sciences*, *66*(6), 1489–1506. https://doi.org/10.1175/2008JAS2636.1

Park, S., Bretherton, C., & Rasch, P. (2014). Integrating cloud processes in the community atmosphere model, version 5. *Journal of Climate*, *27*(18), 6821–6856. https://doi.org/10.1175/JCLI-D-14-00087.1

Qin, Y., Lin, Y., Xu, S., Ma, H.-Y., & Xie, S. (2018). A diagnostic PDF cloud scheme to improve subtropical low clouds in NCAR Community Atmosphere Model (CAM5). *Journal of Advances in Modeling Earth Systems*, *10*(2), 320–341. https://doi.org/10.1002/2017MS001095

Quaas, J. (2012). Evaluating the "critical relative humidity" as a measure of subgrid-scale variability of humidity in general circulation model cloud cover parameterizations using satellite data. *Journal of Geophysical Research*, *117*(D9). https://doi.org/10.1029/2012JD017495

Read, W., Lambert, A., Bacmeister, J., Cofield, R., Christensen, L., Cuddy, D., et al. (2007). Aura Microwave Limb Sounder upper tropospheric and lower stratospheric H2O and relative humidity with respect to ice validation. *Journal of Geophysical Research*, *112*(D24), D24S35. https://doi.org/10.1029/2007JD008752

Schneider, T., Teixeira, J., Bretherton, C., Brient, F., Pressel, K., Schär, C., & Siebesma, A. (2017). Climate goals and computing the future of clouds. *Nature Climate Change*, *7*(1), 3–5. https://doi.org/10.1038/nclimate3190

Shell, K., Kiehl, J., & Shields, C. (2008). Using the radiative kernel technique to calculate climate feedbacks in NCAR's Community Atmospheric Model. *Journal of Climate*, *21*(10), 2269–2282. https://doi.org/10.1175/2007jcli2044.1

Soden, B., Held, I., Colman, R., Shell, K., Kiehl, J., & Shields, C. (2008). Quantifying climate feedbacks using radiative kernels. *Journal of Climate*, *21*(14), 3504–3520. https://doi.org/10.1175/2007JCLI2110.1

Sundqvist, H. (1978). A parameterization scheme for non-convective condensation including prediction of cloud water content. *Quarterly Journal of the Royal Meteorological Society*, *104*(441), 677–690. https://doi.org/10.1002/qj.49710444110

Sundqvist, H., Berge, E., & Kristjánsson, J. (1989). Condensation and cloud parameterization studies with a mesoscale numerical weather prediction model. *Monthly Weather Review*, *117*(8), 1641–1657. https://doi.org/10.1175/1520-0493(1989)117<1641:CACPSW>2.0.CO;2

Tiedtke, M. (1989). A comprehensive mass flux scheme for cumulus parameterization in large-scale models. *Monthly Weather Review*, *117*(8), 1779–1800. https://doi.org/10.1175/1520-0493(1989)117<1779:ACMFSF>2.0.CO;2

Tompkins, A. (2002). A prognostic parameterization for the subgrid-scale variability of water vapor and clouds in large-scale models and its use to diagnose cloud cover. *Journal of the Atmospheric Sciences*, *59*(12), 1917–1942. https://doi.org/10.1175/1520-0469(2002)059<1917:APPFTS>2.0.CO;2

Van Weverberg, K., Boutle, I., Morcrette, C., & Newsom, R. (2016). Towards retrieving critical relative humidity from ground-based remote-sensing observations: Retrieving RHcrit from lidar. *Quarterly Journal of the Royal Meteorological Society*, *142*(700), 2867–2881. https://doi.org/10.1002/qj.2874

Wang, X. (2022a). Role of cloud subgrid-scale structure in modulating clouds viewed by ISCCP, MODIS, and MISR simulators. *Journal of Geophysical Research: Atmospheres*, *127*(11), e2021JD036378. https://doi.org/10.1029/2021JD036378

Wang, X. (2022b). Radiative kernels calculated using RRTMG with input fields from control aquaplanet climate [Dataset]. Zenodo. https://doi.org/10.5281/zenodo.6596656

Wang, X., Liu, Y., Bao, Q., & Wu, G. (2015). Comparisons of GCM cloud cover parameterizations with cloud-resolving model explicit simulations. *Science China Earth Sciences*, *58*(4), 604–614. https://doi.org/10.1007/s11430-014-4989-y

Wang, X., Liu, Y., Wu, G., Lin, S.-J., & Bao, Q. (2013). The application of flux-form semi-Lagrangian transport scheme in a spectral atmosphere model. *Advances in Atmospheric Sciences*, *30*(1), 89–100. https://doi.org/10.1007/s00376-012-2039-2

Wang, X., Miao, H., Liu, Y., & Bao, Q. (2021). Dependence of cloud radiation on cloud overlap, horizontal inhomogeneity, and vertical alignment in stratiform and convective regions. *Atmospheric Research*, *249*, 105358. https://doi.org/10.1016/j.atmosres.2020.105358

Wang, X., & Zhang, M. (2013). An analysis of parameterization interactions and sensitivity of single-column model simulations to convection schemes in CAM4 and CAM5. *Journal of Geophysical Research: Atmospheres*, *118*(16), 8869–8880. https://doi.org/10.1002/jgrd.50690

Wang, X., & Zhang, M. (2014). Vertical velocity in shallow convection for different plume types. *Journal of Advances in Modeling Earth Systems*, *6*(2), 478–489. https://doi.org/10.1002/2014MS000318

Xie, S., Lin, W., Rasch, P. J., Ma, P.-L., Neale, R., Larson, V. E., et al. (2018). Understanding cloud and convective characteristics in version 1 of the E3SM atmosphere model. *Journal of Advances in Modeling Earth Systems*, *10*, 2618–2644. https://doi.org/10.1029/2018MS001350

Xu, K.-M., & Krueger, S. (1991). Evaluation of cloudiness parameterizations using a cumulus ensemble model. *Monthly Weather Review*, *119*(2), 342–367. https://doi.org/10.1175/1520-0493(1991)119<0342:EOCPUA>2.0.CO;2

Xu, K.-M., & Randall, D. (1996a). A semiempirical cloudiness parameterization for use in climate models. *Journal of the Atmospheric Sciences*, *53*(21), 3084–3102. https://doi.org/10.1175/1520-0469(1996)053<3084:ASCPFU>2.0.CO;2

Xu, K.-M., & Randall, D. (1996b). Evaluation of statistically based cloudiness parameterizations used in climate models. *Journal of the Atmospheric Sciences*, *53*(21), 3103–3119. https://doi.org/10.1175/1520-0469(1996)053<3103:EOSBCP>2.0.CO;2

Zelinka, M., Klein, S., & Hartmann, D. (2012). Computing and partitioning cloud feedbacks using cloud property histograms. Part I: Cloud radiative kernels. *Journal of Climate*, *25*(11), 3715–3735. https://doi.org/10.1175/JCLI-D-11-00248.1

Zelinka, M., Myers, T., McCoy, D., Po-Chedley, S., Caldwell, P., Ceppi, P., et al. (2020). Causes of higher climate sensitivity in CMIP6 models. *Geophysical Research Letters*, *47*(1), e2019GL085782. https://doi.org/10.1029/2019GL085782

Zhang, M., Hack, J., Kiehl, J., & Cess, R. (1994). Diagnostic study of climate feedback processes in atmospheric general circulation models. *Journal of Geophysical Research*, *99*(D3), 5525–5537. https://doi.org/10.1029/93JD03523

Zhang, M., Lin, W., Bretherton, C., Hack, J., & Rasch, P. (2003). A modified formulation of fractional stratiform condensation rate in the NCAR Community Atmosphere Model (CAM2). *Journal of Geophysical Research*, *108*(D1), 4035. https://doi.org/10.1029/2002JD002523

Zhou, L., Bao, Q., Liu, Y., Wu, G., Wang, W.-C., Wang, X., et al. (2015). Global energy and water balance: Characteristics from Finite-volume Atmospheric Model of the IAP/LASG (FAMIL1). *Journal of Advances in Modeling Earth Systems*, *7*(1), 1–20. https://doi.org/10.1002/2014MS000349